

Uniwersytet Śląski  
Wydział Matematyki Fizyki i Chemii

Michał Januszewski  
224940

Praca magisterska

# Anomalous transport processes in Josephson junctions

Promotor:  
prof. dr hab. Jerzy Łuczka

Katowice, 2010

|   |   |
|---|---|
| Imię i nazwisko autora pracy            | Michał Januszewski  |
| Imię i nazwisko promotora pracy         | Jerzy Łuczka  |
| Wydział / Jednostka niebędąca Wydziałem | Wydział Matematyki, Fizyki i Chemii / Instytut Fizyki                                     |
| Kierunek studiów                        | fizyka magisterska  |
| Specjalność                             | fizyka teoretyczna  |
| Tytuł pracy                             | Procesy anomalnego transportu w złączach Josephsona                                       |
| Słowa kluczowe (max. 5)                 | złącze Josephsona, transport, karta graficzna, anomalna ruchliwość, cząsteczka Brownowska |

Wyrażam zgodę na udostępnienie mojej pracy dyplomowej (licencjackiej lub magisterskiej) dla celów naukowo–badawczych.

Wyrażam zgodę na rozpowszechnianie pracy poprzez publiczne udostępnianie w wersji drukowanej i elektronicznej w taki sposób, aby każdy mógł mieć do niej dostęp w miejscu, w którym praca jest przechowywana tj. w Archiwum Uniwersytetu Śląskiego lub w Bibliotece Uniwersytetu Śląskiego.

Wyrażam zgodę na rozpowszechnianie pracy poprzez publiczne udostępnienie pracy w wersji elektronicznej w sieci Internet w domenie us.edu.pl oraz w innych serwisach internetowych, tworzonych z udziałem Uniwersytetu Śląskiego.

DATA: .....

PODPIS AUTORA: .....

### Oświadczenie autora pracy

Świadomy odpowiedzialności prawnej oświadczam, że niniejsza praca dyplomowa została napisana przeze mnie samodzielnie i nie zawiera treści uzyskanych w sposób niezgodny z obowiązującymi przepisami.

Oświadczam również, że przedstawiona praca nie była wcześniej przedmiotem procedur związanych z uzyskaniem tytułu zawodowego w wyższej uczelni.

Oświadczam ponadto, że niniejsza wersja pracy jest identyczna z załączoną wersją elektroniczną.

Data

Podpis autora pracy

## **Streszczenie**

Praca zawiera analizę procesów anomalnego transportu w pojedynczym złączu Josephsona w modelu Stewarta-McCumbera oraz w układzie dwóch przetłumionych złącz połączonych za pomocą opornika lub dyfuzyjnego prądu kwazicząstek. Dzięki numerycznym symulacjom stochastycznych równań różniczkowych opisujących dynamikę fazy złącz w obecności fluktuacji termicznych, zidentyfikowane zostały trzy efekty: ujemna przewodność, nieliniowa ujemna przewodność oraz różniczkowa ujemna przewodność. Obliczenia numeryczne zostały przeprowadzone przy użyciu popularnych komputerowych kart graficznych z wykorzystaniem środowiska CUDA. Pokazano, że efekty ujemnej mobilności w układach dynamicznych z szumem mogą być indukowane lub wzmacniane przez fluktuacje termiczne, lecz ich występowanie jest zawsze powiązane z deterministyczną dynamiką systemu bez szumu.

Praca jest zorganizowana w taki sposób, aby możliwe było jej zrozumienie przez czytelników nie zajmujących się tematyką złącz Josephsona oraz procesów anomalnego transportu. Zamieszczono w niej krótkie wprowadzenie do stochastycznych równań różniczkowych oraz do dynamiki złącz Josephsona, w zakresie potrzebnym do zrozumienia prezentowanych wyników. W pracy podkreślono użycie nowoczesnego sprzętu komputerowego, który pozwolił na wykonanie obliczeń ponad 700 razy szybciej niż byłoby to możliwe przy użyciu tradycyjnych metod. Oprogramowanie użyte w pracy zostało opublikowane jako osobny projekt open source ([sdepypy](#)) i pokrótko opisane w pracy w nadziei, że będzie ono przydatne dla czytelników zajmujących się problematyką stochastycznych systemów dynamicznych.

## Abstract

This thesis presents an analysis of anomalous transport processes in a single Josephson junction in the Stewart-McCumber model and in a system of two overdamped junctions coupled by a resistive shunt or a quasiparticle diffusion current. Multiple effects were identified (absolute negative conductance, non-linear negative conductance and negative differential conductance) using extensive numerical simulations of stochastic differential equations describing the phase dynamics of the junctions in the presence of thermal fluctuations. The calculations were performed on Graphics Processing Units with CUDA. It was demonstrated that negative mobility effects in noisy dynamical systems can sometimes be induced or intensified by thermal fluctuations, but their presence is always linked with the deterministic dynamics of the system in the noiseless case.

The thesis is designed so that its main points can be understood by non-specialists. It contains a concise introduction to stochastic calculus and the dynamics of weak links, to the extent necessary to understand the presented results. The use of modern graphics cards, which made it possible to complete the calculations more than 700 times faster than with more traditional hardware, is highlighted. The software used for the simulations has been published as a separate open source project (`sdepy`) and is briefly described in the thesis in the hope that it might prove to be useful in other research involving stochastic dynamical systems.

## Glossary

**AC** Alternating Current

**ANM** Absolute Negative Mobility

**CPU** Central Processing Unit

**CUDA** Compute Unified Device Architecture

**DC** Direct Current

**FPE** Fokker-Planck Equation

**GPGPU** General Purpose computing on Graphics Processing Units

**GPU** Graphics Processing Unit

**GWN** Gaussian White Noise

**JJ** Josephson Junction

**NDM** Negative Differential Mobility

**NNM** Negative Nonlinear Mobility

**ODE** Ordinary Differential Equation

**RAM** Random Access Memory

**RCSJ** Resistively-Capacitively Shunted Junction

**RK2** Runge-Kutta method of the second order

**RTCG** Run-Time Code Generation

**SDE** Stochastic Differential Equation

**SM** Streaming Multiprocessor

**SRK2** Stochastic Runge-Kutta method of the second order

# Contents

|   |            |
|---|------------|
| <b>Streszczenie</b>   | <b>ii</b>  |
| <b>Abstract</b>   | <b>iii</b> |
| <b>Glossary</b>   | <b>iv</b>  |
| <b>1 Introduction</b>   | <b>1</b>   |
| 1.1 Subject of the thesis . . . . .   | 1          |
| 1.2 Outline . . . . .   | 2          |
| <b>2 Stochastic differential equations and their numerical solution</b>       | <b>3</b>   |
| 2.1 Probability theory preliminaries . . . . .                                | 3          |
| 2.2 The Wiener process and white noise . . . . .                              | 3          |
| 2.3 Langevin equations . . . . .  | 5          |
| 2.3.1 Noise number reduction . . . . .  | 5          |
| 2.4 Motion of a Brownian particle and its characterization . . . . .          | 6          |
| 2.4.1 Response to a bias force . . . . .                                      | 7          |
| 2.5 Stochastic differential equations . . . . .                               | 8          |
| 2.6 Numerical integration of stochastic differential equations . . . . .      | 10         |
| 2.6.1 Convergence . . . . .   | 11         |
| 2.6.2 The stochastic Euler method . . . . .                                   | 12         |
| 2.6.3 The stochastic Runge-Kutta method of the second order . . . . .         | 12         |
| <b>3 General purpose computing with Graphics Processing Units</b>             | <b>14</b>  |
| 3.1 GPU programming using CUDA . . . . .                                      | 15         |
| 3.2 Numerical solution of stochastic differential equations on GPUs . . . . . | 17         |
| <b>4 Dynamics of weak links</b>   | <b>19</b>  |
| <b>5 Single AC-driven Josephson junction</b>                                  | <b>25</b>  |
| 5.1 Deterministic dynamics . . . . .  | 25         |
| 5.2 Impact of noise . . . . .   | 29         |
| 5.3 Interpretation in the Stewart-McCumber model . . . . .                    | 34         |
| 5.4 Note on previous work . . . . .   | 35         |

|   |           |
|---|-----------|
| <b>6 Two overdamped AC-driven Josephson junctions</b>     | <b>36</b> |
| 6.1 Resistive shunt coupling . . . . .                    | 37        |
| 6.2 Quasiparticle coupling . . . . .                      | 41        |
| 6.3 Identical junctions . . . . .                         | 43        |
| 6.3.1 Dynamics overview . . . . .                         | 43        |
| 6.3.2 AC driving applied to a single junction . . . . .   | 43        |
| 6.3.3 AC driving applied to both junctions . . . . .      | 53        |
| 6.4 Two different junctions . . . . .                     | 56        |
| 6.5 Interpretation in the RSJ model . . . . .             | 59        |
| 6.6 More than two overdamped junctions . . . . .          | 60        |
| <b>7 Summary</b>  | <b>61</b> |
| <b>Appendices</b>   | <b>62</b> |
| <b>A The sdepsy software package</b>                      | <b>64</b> |
| A.1 General architecture of <code>sdepsy</code> . . . . . | 64        |
| A.2 Optimization techniques . . . . .                     | 67        |
| A.3 Summary and future work . . . . .                     | 68        |
| <b>Bibliography</b>                                       | <b>69</b> |

# 1 Introduction

Over the last 50 years, Josephson Junctions (JJs) formed by two weakly coupled superconductors have attracted considerable interest due to their many practical applications. They also have the remarkable property of being describable using very simple mathematics, and are one of the few physical systems where quantum effects can be readily observed on the macroscopic scale.

In this thesis, we will be working with the Stewart-McCumber model of a JJ, which describes the current-voltage characteristics of the junction using lumped electrical elements such as resistors, capacitors, and current sources. The equations of this model can be used to describe a multitude of different physical systems including, among others, Brownian particles moving in a sinusoidal spatial potential. In 2007, it was discovered that such particles can exhibit multiple anomalous transport phenomena – in particular, they can move against a static bias force in the presence of thermal fluctuations. In the JJ interpretation, this corresponds to the phenomenon of absolute negative conductance.

Throughout this thesis we will discuss the analyzed systems primarily in terms of Brownian particles. Josephson junctions will be used as a convenient physical system which can:

- provide a physical motivation for the Brownian particle models,
- be used to experimentally verify the results.

The Brownian particle description is commonly used as it provides a simple interpretation of the underlying equations – one that is easy to understand and visualize, and which refers to objects described by the intuitive laws of classical mechanics.

## 1.1 Subject of the thesis

The goal of this thesis is to investigate anomalous transport effects in simple classical systems of Brownian particles. Of particular importance will be systems that are mathematically minimal and which model the phase dynamics of Josephson junctions, which makes it possible to easily test numerical and theoretical predictions in an experimental setting. Our primary aim will be to identify parameter regimes where at least one of the particles exhibits negative mobility by moving against an external bias force (see Chapter 2 for a more detailed explanation). The thesis can also be seen as an independent confirmation of the results presented by Machura et al. [30] and Speer et al. [46] in 2007,

as well as an extension of their work to systems of coupled JJs.

A secondary aim of the thesis is to show how to effectively perform stochastic simulations using modern computer hardware.

## 1.2 Outline

This thesis is organized as follows. In Chapter 2 we review some fundamental definitions and results from the area of stochastic calculus. We show their usefulness as a mathematical description of Brownian particles, and outline some simple numerical methods for solving Stochastic Differential Equations (SDEs). We continue looking at this topic from a technical standpoint in Chapter 3, where we show how modern computing hardware in general, and Graphics Processing Units (GPUs) in particular can be used to greatly accelerate calculations of the kind that are interesting for us in this work. In Chapter 4 we briefly discuss the physics of JJs and introduce their dynamical model that is used in the remaining part of the thesis. In the following two chapters we investigate the transport properties of Brownian particle systems modeling a single junction, and two junctions, respectively. We focus our attention on the counterintuitive effects of negative mobility in mathematically minimal systems, that is systems with a three-dimensional phase space, which is known to be a requirement for the existence of deterministic chaos [42], and which in turn seems to be crucial for the presence of some of the negative mobility effects [27]. In Chapter 7 we provide a concise summary of the obtained results and discuss their potential applications and future work. The thesis is concluded by Appendix A, where we provide a description of the software that was developed and used for all numerical calculations.

## 2 Stochastic differential equations and their numerical solution

Throughout this chapter we will be working with Kolmogorov's axiomatic definition of probability. We assume some fundamental concepts of probability theory (such as probability densities, random variables, etc.) to be known to the reader, but no prior knowledge of stochastic calculus will be required. We begin by establishing notation and defining a few basic mathematical objects.

### 2.1 Probability theory preliminaries

We define a *probability space* as a triple  $(\Omega, \mathcal{F}, P)$ , where  $\Omega$  is a sample space,  $\mathcal{F}$  is a  $\sigma$ -algebra of events (subsets of the sample space), and  $P: \mathcal{F} \rightarrow [0; 1]$  is a probability measure.

A *stochastic process* can then be defined as  $\mathcal{X} = \{X(t): t \in T\}$ ,  $\mathcal{X}: T \times \Omega \rightarrow \mathbb{R}$  – a family of random variables indexed by a set  $T$  („time”), which can be finite or infinite. In this thesis, we will only work with stochastic processes with  $T = \mathbb{R}$ , known as *continuous-time stochastic processes*. When taken at a specific time instant  $t \in T$ , a stochastic process becomes a random variable  $X(t) = \mathcal{X}(t, \cdot)$ . If the time is allowed to vary, but the event  $\omega$  is set:  $\mathcal{X}(\cdot, \omega): T \rightarrow \mathbb{R}$ , we get a *realization* of the stochastic process, also known as a *sample path* or *trajectory*.

Given a stochastic process we can calculate its *autocorrelation function*

$$r(t, s) = E[X(t)X(s)]. \quad (2.1)$$

If the autocorrelation is only a function of  $|t - s|$ , we denote it by  $c(|t - s|) = r(t, s)$  and call the stochastic process *stationary*. It is then possible to define its *spectral density* as

$$S(\omega) = \int_{-\infty}^{\infty} c(s) \exp(-i\omega s) ds. \quad (2.2)$$

### 2.2 The Wiener process and white noise

Of particular importance to our considerations in this thesis will be the Wiener stochastic process, which was originally proposed as a mathematical model of Brownian motion,

i.e. the random motion of a particle suspended in a fluid. The Wiener process has since found many other applications, both in pure mathematics, and in applied fields of science, such as economics [3].

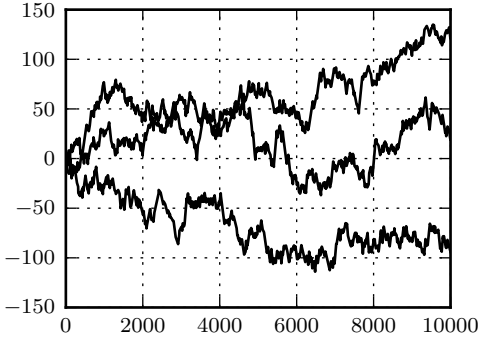


Figure 2.1: Three independent realizations of a Wiener process.

$E[W(t)] = 0$ . It can also be shown that sample paths of a Wiener process are almost surely continuous, nowhere differentiable functions of time [14] (see Figure 2.1), and that  $\lim_{t \rightarrow \infty} W(t)/t = 0$  with probability one [26]. The autocorrelation of a Wiener process can be calculated as

$$\begin{aligned} r(t, s) &= E[W(t)W(s)] = E[(W(s) + W(t) - W(s))W(s)] = \\ &= E[W^2(s)] + E[(W(t) - W(s))W(s)] = \\ &= s + E[W(t) - W(s)]E[W(s)] = s, \quad t \geq s \geq 0, \end{aligned}$$

or more generally  $r(t, s) = \min(t, s)$ .

We can now define the derivative of the Wiener process

$$\xi(t) = \frac{dW(t)}{dt}. \quad (2.5)$$

The autocorrelation of this new process is

$$r(t, s) = E \left[ \frac{dW(t)}{dt} \frac{dW(s)}{ds} \right] = \frac{\partial}{\partial t \partial s} E[W(t)W(s)] = \frac{\partial}{\partial t \partial s} \min(t, s) = \delta(t - s). \quad (2.6)$$

Using this in Eq. (2.2) allows us to calculate the spectral density

$$S(\omega) = \int_{-\infty}^{\infty} \delta(s) \exp(-i\omega s) ds = 1. \quad (2.7)$$

By analogy to signal theory, we call the derivative of the Wiener process *Gaussian White Noise (GWN)*. It is a zero-mean, stationary process with a constant, non-zero spectral density. However, due to the non-differentiability of the paths of the Wiener process, GWN is not a stochastic process in the usual sense. It also cannot be realized physically, as its flat spectrum would imply infinite energy [14]. It is however a good approximation of colored noise processes (noises with broad-banded, but finite spectra dependent on frequency), for which the autocorrelation at different time instants has been made arbitrarily small.

## 2.3 Langevin equations

Having defined GWN, we will now want to describe the dynamics of a Brownian particle in a way that would allow us to merge the usual deterministic description with a stochastic one. One way to do that is to add some *noise terms* to the usual Newtonian equation of motion

$$m\ddot{x} + \gamma\dot{x} = A(x, t) + B(x, t)\Gamma(t), \quad (2.8)$$

where  $\Gamma(t)$  is a noise term and the dot represents a time derivative. In particular,  $\Gamma(t)$  could be the GWN defined in Eq. (2.5), in which case we will denote it by  $\xi(t)$ .

The motivation behind this approach is as follows. We consider the system we want to model as having both fast and slow degrees of freedom. The slow ones we know exactly how to model, and we include them explicitly in the  $A(x, t)$  term. The fast ones are assumed to be unknown and we replace them by the Stokesian friction term  $\gamma\dot{x}$  and the random noise  $\Gamma(t)$ .

In this thesis we will only be concerned with the GWN, which is a good first approximation for many practical physical systems of Brownian particles. For this type of noise, the form of  $B(x, t)$  in Eq. (2.8) is given by the so-called Einstein relation:

$$B(x, t) = \sqrt{2\gamma k_B T}, \quad (2.9)$$

where  $k_B$  is the Boltzmann constant,  $T$  is the temperature and  $\gamma$  is the Stokes friction coefficient. This relation can be proven using the fluctuation-dissipation theorem [45].

### 2.3.1 Noise number reduction

When dealing with equations with multiple white noise terms it often makes sense to try to reduce the number of independent noise sources – both for increased clarity of the formulas and for numerical efficiency (generation of normal variates is a computationally costly process). Taking into consideration that the sum of two independent normally distributed random variables  $X \sim N(\mu, \sigma^2)$  and  $Y \sim N(\nu, \tau^2)$  is also a normally distributed random variable  $Z = X + Y \sim N(\mu + \nu, \sigma^2 + \tau^2)$  (which can be easily proven

using characteristic functions [14]), the following reduction rules can be written for two independent,  $\delta$ -correlated noise sources  $\xi_1(t)$  and  $\xi_2(t)$ :

$$A\xi_1(t) \pm B\xi_1(t) = (A \pm B)\xi_1(t), \quad (2.10)$$

and

$$A\xi_1(t) \pm B\xi_2(t) = \sqrt{A^2 + B^2}\xi_3(t), \quad (2.11)$$

where  $\xi_3(t)$  is another  $\delta$ -correlated noise source.

These rules can be easily checked by requiring the autocorrelations of the left and right hand sides of the equations at times  $t$  and  $t'$  to be equal. For instance, for Eq. (2.11)

$$\begin{aligned} \langle (A\xi_1(t) \pm B\xi_2(t)) (A\xi_1(t') \pm B\xi_2(t')) \rangle &= A^2\langle \xi_1(t)\xi_1(t') \rangle + B^2\langle \xi_2(t)\xi_2(t') \rangle \\ &= (A^2 + B^2)\delta(t - t'), \end{aligned}$$

where the correlation between  $\xi_1(t)$  and  $\xi_2(t')$  vanishes by the assumption of independence of these noise sources.

## 2.4 Motion of a Brownian particle and its characterization

In this thesis we aim to analyze transport processes that take place within systems of Brownian particles. A transport process can be intuitively understood as a process that results in the movement of some physical quantity, such as mass, energy, charge or momentum from one place to another. The Brownian particle in our case acts as the vessel with which the quantity being moved is associated. We generally will prefer to work with abstract models that do not specify what that quantity is. This is justified, as frequently the same mathematical model can be applied to different physical systems so that working with an abstract model allows us to attain a higher level of generality.

There are a number of simple quantities that can be used to characterize the motion of a Brownian particle (and thus the associated transport process), such as:

- its average velocity

$$\langle v \rangle = \left\langle \lim_{t \rightarrow \infty} \frac{1}{t} \int_0^t dt' \dot{x}(t') \right\rangle, \quad (2.12)$$

- its effective diffusion coefficient

$$D_{\text{eff}} = \lim_{t \rightarrow \infty} \frac{\langle x^2(t) \rangle - \langle x(t) \rangle^2}{2t}, \quad (2.13)$$

- or the variance of its velocity

$$\sigma_v^2 = \langle v^2 \rangle - \langle v \rangle^2. \quad (2.14)$$

In all of the above formulas the brackets on the right hand sides denote ensemble-averaging. The effective diffusion coefficient and the variance of velocity are measures of the spread of the particle's position and velocity, respectively. As such, they provide data about the efficiency of the transport, but do not give any indication as to its direction, which in turn can be determined from the average velocity  $\langle v \rangle$ . The average velocity will be the primary quantity of interest in this thesis, so we will now look at it more closely.

If the analyzed system is ergodic, the time- and ensemble-averaging become equivalent and one of them is superfluous. Equation (2.12) can then be simplified to

$$\langle v \rangle = \lim_{t \rightarrow \infty} \frac{x(t) - x(0)}{t} = \lim_{t \rightarrow \infty} \frac{x(t)}{t}, \quad (2.15)$$

where we skipped the ensemble-averaging, carried out the integration, and neglected the term  $x(0)/t$  which approaches 0 as  $t \rightarrow \infty$ .

When estimating  $\langle v \rangle$  from the results of numerical calculations both averages are kept:

$$\langle v \rangle \approx \langle v \rangle_{\text{sim}} = \left\langle \frac{x(t_f) - x(t_i)}{t_f - t_i} \right\rangle. \quad (2.16)$$

This is justified as it greatly reduces the time needed to estimate the average velocity – instead of performing a single lengthy simulation, multiple shorter paths can be calculated in parallel.

The time-average in Eq. (2.16) is performed over a large, but finite time period  $T = t_f - t_i$ . For systems driven by a periodic force, several thousand periods of the driving force are usually enough.  $t_i$  is typically chosen larger than 0 so that any initial transients in the system die out before the  $\langle v \rangle$  estimate is calculated.

#### 2.4.1 Response to a bias force

Consider Eq. (2.8) with  $A(x, t) = a(x, t) + F$ , such that  $a(x, t)$  is spatially periodic and symmetric (that is  $a(x, t) = a(x + L, t)$  where  $L$  is the spatial period), and such that the time-dependence is a single harmonic. If  $F = 0$ , there is no preferred direction of motion and we expect the particle's mean position to stay constant and  $\langle v \rangle = 0$ . If the constant external force  $F$  is set to a non-zero value, the symmetry of the system is broken and directed motion can be expected to arise. The *mobility* of the particle can then be defined as

$$\mu = \frac{\langle v \rangle}{F}. \quad (2.17)$$

For small  $F$ , the mobility  $\mu$  is independent of the force, which is called the *linear response*. This does not hold true for higher values of  $F$ , in which case the system is said to be in the *nonlinear response* regime [45].

Typically, the mobility  $\mu$  is expected to be positive – i.e. the particle should on average move in the direction pointed to by the force  $F$ . If it moves in the opposite direction, the mobility becomes negative and we say that the system exhibits the counterintuitive phenomenon of *anomalous transport*. If  $\mu < 0$  in the neighborhood of  $F = 0$ , the effect is called Absolute Negative Mobility (ANM) (see Figure 2.2b). Away from  $F = 0$  we refer to it as Negative Nonlinear Mobility (NNM). Both effects eventually disappear for high enough values of  $F$ .

A somewhat similar, though much more common phenomenon is Negative Differential Mobility (NDM), in which the differential mobility  $d\langle v \rangle / dF$  becomes negative. In this thesis we will mainly be interested in the more rare and surprising effects of ANM and NNM.

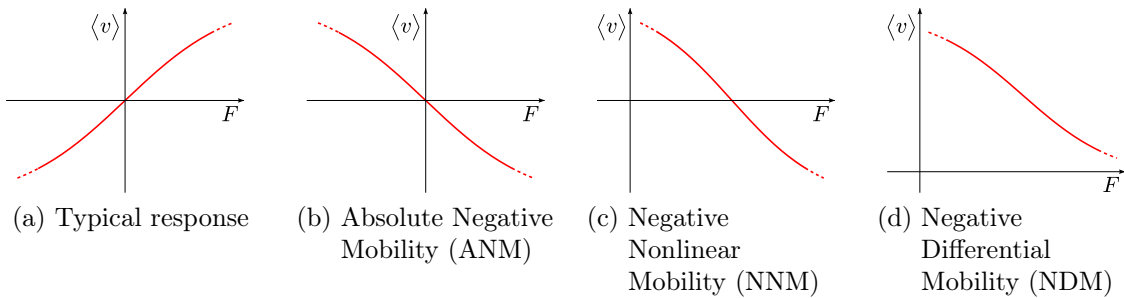


Figure 2.2: Response of a Brownian particle to a constant load force  $F$ .

The negative mobility effects might appear to violate the laws of thermodynamics – after all, if a system is in thermal equilibrium, its reaction to an external bias force should be in the direction of that force (Le Chatelier’s principle). This reasoning however does not apply if the system is out of equilibrium, which can be ensured e.g. by applying an unbiased, oscillating driving force.

## 2.5 Stochastic differential equations

Consider the following first order Langevin equation:

$$\frac{dx}{dt} = a(x, t) + b(x, t)\xi(t), \quad (2.18)$$

with  $\langle \xi(t) \rangle = 0$  and  $\langle \xi(t)\xi(s) \rangle = \delta(t-s)$ . The  $\xi(t)$  here is called a *multiplicative noise* due to the dependence of the  $b(x, t)$  term on  $x$ . If  $b$  were to depend on  $t$  only, the noise would be called an *additive noise*. The deterministic term  $a(x, t)$  is known as the *drift coefficient* and the stochastic factor  $b(x, t)$  as the *diffusion coefficient*.

So far we have assumed Eq. (2.18) to be a well-defined mathematical object, which is not really the case due to the non-existence of  $\xi(t)$ . The Langevin equation in question

is properly interpreted in terms of the stochastic integral equation

$$x(t) - x(0) = \int_0^t a(x(s), s) ds + \int_0^t b(x(s), s) \xi(s) ds, \quad (2.19)$$

which can be rewritten as

$$x(t) - x(0) = \int_0^t a(x(s), s) ds + \int_0^t b(x(s), s) dW(s) \quad (2.20)$$

using Eq. (2.5).

In this form, the only mathematical object that requires some further comments is the second integral in Eq. (2.20). We consider the stochastic integral  $I = \int_t^{t'} G(s) dW(s)$  to be defined by analogy to the Riemann-Stieltjes integral as the limit of the approximating sum

$$\lim_{n \rightarrow \infty} S_n = \lim_{n \rightarrow \infty} \sum_{i=1}^n G(\tau_i) (W(t_i) - W(t_{i-1})),$$

with  $\tau_i = \alpha t_i + (1 - \alpha)t_{i-1}$  defining the partition of the interval  $[t, t']$ . In classical deterministic calculus it can be shown that such a definition does not depend on the choice of  $\alpha$ . In stochastic calculus however this is not the case and multiple interpretations of the stochastic integral can be given [26]. The two most commonly used ones are  $\alpha = 0$  (Itô interpretation) and  $\alpha = 1/2$  (Stratonovich interpretation).

In the Itô interpretation Eq. (2.18) is written as the following SDE:

$$dx = a(x, t) dt + b(x, t) dW(t). \quad (2.21)$$

If a change of variables  $y = y(x(t), t)$  is required, it can be done using the following formula [14]:

$$\begin{aligned} dy &= \frac{\partial y}{\partial t} dt + \frac{\partial y}{\partial x} dx + \frac{1}{2} \frac{\partial^2 y}{\partial x^2} b^2 dt = \\ &= \left( \frac{\partial y}{\partial t} dt + \frac{\partial y}{\partial x} a + \frac{1}{2} \frac{\partial^2 y}{\partial x^2} b^2 \right) dt + \frac{\partial y}{\partial x} b dW(t). \end{aligned}$$

The same equation can also be written in the Stratonovich interpretation

$$dx = a(x, t) dt + b(x, t) \circ dW(t), \quad (2.22)$$

in which case the change of variables can be performed using [14]

$$\begin{aligned} dy &= \frac{\partial y}{\partial t} dt + \frac{\partial y}{\partial x} \circ dx = \\ &= \left( \frac{\partial y}{\partial t} dt + \frac{\partial y}{\partial x} a \right) dt + \frac{\partial y}{\partial x} b \circ dW(t). \end{aligned}$$

In order for our Langevin description to be complete, we generally need to specify which interpretation of stochastic calculus is being used. In our case however it turns out that we can avoid answering this question altogether. It can be shown that the Itô SDE (2.21) is equivalent to the following Stratonovich SDE [14]:

$$dx = \left( a(x, t) - \frac{1}{2}c(x, t) \right) dt + b(x, t) \circ dW(t), \quad (2.23)$$

with  $c(x, t) = \frac{\partial b(x, t)}{\partial x} b(x, t)$ . The two interpretations are therefore equivalent, up to a shift in the drift term. If we now recall that we are only using systems with additive GWN for which the diffusion coefficient is a constant given by Eq. (2.9), we see that the Itô and Stratonovich interpretation of Eq. (2.18) are equivalent.

## 2.6 Numerical integration of stochastic differential equations

There are two generic approaches to the numerical solution of SDEs:

- calculate the evolution of the probability density,
- calculate the evolution of individual realizations.

In the first group, the most prominent methods are the numerical solution of the corresponding Fokker-Planck Equation (FPE) and calculation of the probability density with path integration methods [33].

The FPE is a partial differential equation describing the time evolution of the probability density of the system modeled by an SDE. Its numerical solution is relatively difficult to implement and parallelize to take advantage of modern computer hardware. Path integral methods are easier to implement and parallelize, but their memory and computational power requirements grow very fast with increasing dimensionality of the analyzed problems.

In the second group, the most widely used method is direct Monte Carlo integration, in which a large number of sample paths of a discrete time approximation of the stochastic differential equation is calculated. An ensemble averaging over the results can then be performed to calculate quantities of interest that can be expressed as moments of the probability distribution.

While the probability density function for the system is never explicitly calculated in Monte Carlo integration, it can be approximated by the means of a frequency histogram. This however requires a large number of paths, which can significantly increase the computational time if a precise approximation is required.

From a practical standpoint an important advantage of Monte Carlo integration is the mutual independence of the calculated paths, which makes it a so-called embarrassingly

parallel problem. This fits perfectly with the capabilities of modern computer hardware such as multi-core Central Processing Units (CPUs) or GPUs. This salient feature coupled with the ease of implementation makes Monte Carlo integration a very robust numerical tool for the analysis of SDEs.

Since in this thesis we will mostly be interested in simple averages expressible as moments of the probability distribution and the exact probability distribution will be of a little interest to us, Monte Carlo integration will be our method of choice in the following chapters.

Throughout this section we will be concerned with the numerical, discrete time approximation of the following Langevin equation:

$$\frac{dx}{dt} = f(x, t) + \xi(t), \quad (2.24)$$

with  $\langle \xi(t) \rangle = 0$  and  $\langle \xi(t)\xi(s) \rangle = 2D\delta(t-s)$ .  $\Delta t = t_{n+1} - t_n$  will denote the time step size, and the numerical approximation of  $x(t_n)$  will be denoted as  $X_n$ .

### 2.6.1 Convergence

The first thing that might come to our mind when we try to numerically solve an SDE is to try to use some of the well-known deterministic numerical methods for Ordinary Differential Equations (ODEs), replacing any increments of the Wiener process by normally distributed variates. It turns out however that this approach does not provide any guarantees about the order of convergence of such a method, making it generally useless [26]. The order of convergence for stochastic methods is very often different than the one of similar deterministic methods, so careful convergence analysis is required.

There are two kinds of convergence that are commonly considered when working with numerical methods for SDEs. We say that there is *strong convergence* with order  $\gamma$  if

$$E[|x(t_n) - X_n|] \leq C\Delta t^\gamma, \quad (2.25)$$

where  $C$  is a constant, and where  $\Delta t$  is smaller than some maximum value  $\Delta_0$ . Strong convergence is also called *pathwise convergence*, as it guarantees a degree to which the numerical solution  $X_n$  approximates the paths of the actual stochastic process  $\mathcal{X}$ . If we take the stochastic part in the SDE to be zero, strong convergence reduces to the usual deterministic criterion for an approximation of an ODE.

Sometimes we are only interested in the quantity  $E[g(x(t))]$ , where  $g$  is some function. In this case we need to have a good approximation of the probability distribution of  $x(t_n)$ , but a pathwise approximation is not necessary. A more useful way to estimate the level of convergence is then the *weak convergence*, which we say is of order  $\beta$  if

$$|E[g(x(t_n))] - E[g(X_n)]| \leq C\Delta t^\beta. \quad (2.26)$$

Weak convergence also reduces to the standard definition of convergence for ODEs if the stochastic terms disappear identically and if  $g(x)$  is taken to be  $x$ .

The strong and weak orders of convergence are often different for a numerical method and thus need to be specified separately [26].

### 2.6.2 The stochastic Euler method

The stochastic Euler method, also known as the Euler-Maruyama approximation [26], is the simplest scheme for numerical solution of SDEs. It is formed by fixing the drift and diffusion coefficients to their values at the beginning of each time subinterval:

$$X_{n+1} = X_n + f(X_n, t_n) \Delta t + \sqrt{2D\Delta t} \psi, \quad (2.27)$$

where  $\psi \sim \mathcal{N}(0, 1)$ .

It can be shown that for smooth drift and diffusion coefficients the Euler scheme has a strong order of convergence  $\gamma = 0.5$  and weak order  $\beta = 1.0$  for a general multiplicative noise. If the noise is additive, the strong order of convergence is  $\gamma = 1.0$ .

While the stochastic Euler scheme reduces to the deterministic Euler scheme for ODEs if there is no noise, it should not be considered a proper stochastic generalization of the Euler method. Such a generalization is actually known as the Milstein scheme and it includes in Eq. (2.27) an additional term proportional to  $(\Delta W)^2$ , which makes its strong convergence order  $\gamma = 1.0$  in the general case of multiplicative noise [26].

### 2.6.3 The stochastic Runge-Kutta method of the second order

The Stochastic Runge-Kutta method of the second order (SRK2) for Eq. (2.24) can be written as [18]

$$\begin{aligned} X_{n+1} &= X_n + \frac{1}{2} \Delta t (F_1 + F_2) + \sqrt{2D\Delta t} \psi \\ F_1 &= f(X_n, t_n) \\ F_2 &= f(X_n + \Delta t F_1 + \sqrt{2D\Delta t} \psi, t_n + \Delta t), \end{aligned} \quad (2.28)$$

where  $\psi \sim \mathcal{N}(0, 1)$ . It can be considered to be a stochastic extension of the following variant of Runge-Kutta method of the second order (RK2) for Ordinary Differential Equations [43], known as the Heun method [26]:

$$\begin{aligned} X_{n+1} &= X_n + \frac{1}{2} \Delta t (F_1 + F_2) \\ F_1 &= f(X_n, t_n) \\ F_2 &= f(X_n + \Delta t F_1, t_n + \Delta t). \end{aligned}$$

It should be emphasized that SRK2 is not just a naive extension of RK2. In fact, a number of straightforward extensions of RK2 demonstrably do not work in the stochastic case. For instance, trying to set  $F(x, t) = f(x) + \xi(t)$  fails because  $\xi(t)$  has infinite variance. A different approach, based on extending RK2 to read

$$X_{n+1} = X_n + \frac{1}{2}\Delta t (F_1 + F_2) + \int_0^t \xi(t') dt'$$

while including only terms with finite variance, turns out to have a deterministic portion accurate to order  $\Delta t^2$ , but a stochastic portion accurate only to order  $\Delta t$ . The SRK2 on the other hand is accurate to order  $\Delta t^2$  in both portions.

The SRK2 can be shown to have a weak order of convergence  $\beta = 2.0$  [26]. This is enough for our needs as we are interested in observables expressible as expected values of the position and velocity, and not in the individual trajectories.

Braňka and Hayes compared the SRK2 with a number of other numerical schemes, including one based on the second order stochastic Taylor expansion. The comparisons were done for both one-dimensional [5] and multi-dimensional systems [6]. Their conclusion was that while SRK2 approximates multiple stochastic terms from the expansion with a single random variable, its results are usually good enough for all practical purposes. The only test case where the stochastic expansion algorithm exhibited better convergence was the estimation of the energy of the analyzed system.

It is a known fact that numerical methods using only simple increments of the Wiener process converge with at most a strong order of 1. The stated order of convergence is however always defined for a worst case scenario, and higher order is often possible for specific classes of SDEs, e.g. those with additive noise [7].

Unless noted otherwise, all numerical results presented in this thesis were obtained using the Stochastic Runge-Kutta method of the second order outlined above and implemented in the `sdepy` package (see Appendix A).

### 3 General purpose computing with Graphics Processing Units

In 1965, Gordon Moore observed that the number of transistors that can be placed in an integrated circuit at a fixed cost doubled approximately every two years [32]. This trend, which continued throughout the 20th century and the first decade of the 21st century, became known as Moore's law. The accuracy and applicability of this „law” was ensured by the continued development of semiconductor technologies.

For many years, the increasing number of transistors at the disposal of chip designers translated directly into increases in the speed of computer processors. However, during the second half of the first decade of the 21st century the CPU clock speeds started to level out, hitting a barrier at a few GHz. This barrier arose mainly from the physical limitations of the used technologies – the CPUs could not run any faster due to problems with heat dissipation. Despite the appearances, these issues did not spell out an end to the Moore's law. The number of transistors continued to increase, but they started to be used in a different way – either to construct even more complex computational units, or to simply provide more of those units (*cores*) on a single chip. As this thesis is being written, in mid-2010, a common number of cores for a CPU is 2 or 4.

At the same time, it was noticed that large gains in computational efficiency could potentially be achieved if one were to use the available transistors to build simpler, more specialized processors with a larger number of cores. This was precisely the path taken by the manufacturers of Graphics Processing Units (GPUs) used in computer video cards. GPUs were originally supposed to accelerate common operations in computer graphics, especially ones related to rendering three-dimensional scenes. As their computational power grew, they gained the attention of the scientific community, which tried to use them for numerical computations [44]. This became known as General Purpose computing on Graphics Processing Units (GPGPU), and initially required a fairly extensive knowledge of computer graphics. Numerical problems to be solved using GPUs had to be translated to graphical primitives such as sets of vertices or textures, processed by programs written in a so-called shader language, and then translated back to the original representation.

### 3.1 GPU programming using CUDA

The usage of GPUs was greatly simplified by the introduction of the Compute Unified Device Architecture (CUDA) environment (and subsequently its equivalent open standard – OpenCL). CUDA and OpenCL make it possible to access the computational resources of a GPU from programs written in a language virtually identical to C. CUDA originally referred to the hardware architecture of modern NVIDIA GPUs, but it is now commonly used as the name of both the hardware and its accompanying software stack.

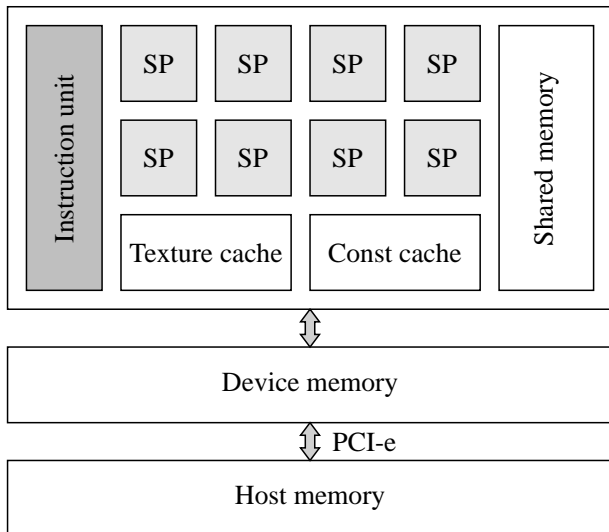


Figure 3.1: A schematic view of the CUDA hardware architecture, depicting a single streaming multiprocessor and different kinds of memory.

From the hardware standpoint, CUDA devices are organized around the concept of a Streaming Multiprocessor (SM). In devices with compute capability 1.3 or lower, a SM consists of 8 scalar processors, a special function unit, instruction cache, and the following types of on-chip memory (see Figure 3.1) [40]:

- a set of 32-bit registers (local per scalar processor),
- a limited amount of shared memory (16 kB, shared between the 8 scalar processors),
- a texture cache (shared, read-only),
- a constant memory cache (shared, read-only).

A single modern GPU contains multiple such SMs. In addition to the on-chip shared memory, the GPU also has a global device memory, which is 5 orders of magnitude larger (several gigabytes). The downside of this type of memory is its access time, which is 2 orders of magnitude longer than that of the on-chip memory of a SM. Global GPU

memory is still much faster in comparison with the host memory, i.e. the ordinary computer Random Access Memory (RAM), to which the GPU does not have direct access. It is easy to see that proper memory management is one of the most important factors determining the speed of a GPU program. There is always a trade-off between speed and size – the fastest memory is the scarcest resource, while the most abundant host memory, while potentially very large, is also prohibitively slow when used from the GPU (due to the throughput and latency of the PCI-e bus used to copy data between the video card and the host). Most basic GPU optimization techniques are therefore based on the concept of keeping as much data as possible in the fastest available memory. The problems with memory management are a general trait of modern computing systems, stemming from the fact that memory clock rates double slower than those of processors, creating an exponentially increasing speed gap between the two.

From the programmer’s point of view, CUDA programs are organized into *kernels*. A kernel is a function that is executed multiple times simultaneously on different SMs. Each instance of this function is called a *thread*, and is assigned to a single scalar processor. Threads are then grouped in one-, two- or three-dimensional *blocks* assigned to multi-processors in an 1-1 manner (1 block – 1 SM). The blocks are organized into a one- or two-dimensional *grid*. The size and dimensionality of the grid and blocks is determined by the programmer at the time of kernel invocation. Knowledge of the grid position, and the in-block position makes it possible to calculate a thread ID that is unique during the kernel execution. Within a single block threads can synchronize their execution and share information through the on-chip shared memory. Synchronization between blocks is not supported in any way other than serializing the execution of kernels.

In addition to the programming model described above, CUDA provides a software stack consisting of a CUDA C compiler, a profiler, a GPU driver, system libraries implementing the CUDA application programming interface and two higher level mathematical libraries (CUBLAS and CUFFT).

Modern GPUs have a peak performance of about 1 TFLOPS, which is however only achieved by single precision calculations. Double precision calculations are an order of magnitude slower, and are not supported on older devices. While this might seem to be a significant limitation for scientific computing, we have found that this is not the case for numerical solution of SDEs of the type investigated in this thesis, provided some precautions are taken (see Appendix A for more information on this).

While programming in CUDA C is fairly easy for anyone familiar with the C programming language, the new programming model usually requires a complete redesign of the algorithms. A concern that is often brought up and which we would like to briefly address here is whether this redesign of algorithms and a potential rewrite of existing code is warranted. One could worry that perhaps this programming model will soon be replaced by a completely new one, at which point the rewritten code could not be used any longer. We believe that this will not be the case, and the reasoning is as follows. Un-

less a breakthrough in electronic technologies is achieved, or unless a complete paradigm shift towards novel computational platforms takes place, computer hardware will in all likelihood continue to evolve towards massively multi-core systems. Due to the trends outlined at the beginning of this chapter, these systems will have a limited amount of very fast memory and a much larger amount of slower storage space. Therefore, we can expect the algorithms designed for the CUDA environment to work quite well on this new hardware.

### 3.2 Numerical solution of stochastic differential equations on GPUs

Numerical solution of SDEs via the Monte Carlo method outlined in Chapter 2 is an example of a so-called embarrassingly parallel problem, which is perfectly suited for a GPU implementation. The method is based on the simultaneous calculation of paths for different realizations of noise, and since the paths are mutually independent, no data sharing needs to take place between them.

To implement the Monte Carlo method in the CUDA environment, we assign each path to a separate kernel. The kernels are grouped into blocks of arbitrary size (typically 64 kernels per block). The exact number does not matter and is chosen to utilize the underlying hardware most efficiently (there are limitations related to the number of registers available in a SM). The size of the grid is then chosen such that the total amount of threads matches the desired number of paths (usually several hundred to several thousand).

To minimize the number of global device memory writes and reads, multiple time steps are calculated in a single kernel invocation. At the beginning of the kernel execution the dynamical variables are loaded from the global memory and cached in local variables. The calculations then proceed using local variables only, and only the final value is written back to the global memory. To further increase the speed of the calculations, hardware-accelerated transcendental functions can be utilized. These functions are provided by the special functions unit in CUDA SMs. Further implementation details are discussed in Appendix A.

Using the approach outlined above a single modern graphics card can provide a 2-3 order of magnitude speed-up as to compared to a single core of a typical CPU [21]. This huge leap in speed makes it possible to interactively investigate problems that previously required lengthy calculations, and to explore much larger areas of the parameter space of various stochastic dynamical systems.

The majority of the numerical calculations described in this thesis was done on the 4-GPU **rider** system at the University of Silesia (four NVIDIA GTX 285 cards with 2 GB of memory each). Some calculations were also performed using the NVIDIA GTX 280

and Tesla C1060 GPUs. All production runs were done on Ubuntu Linux 9.10, using the CUDA 3.0 environment.

## 4 Dynamics of weak links

As we have already mentioned in the previous chapters, the prototypical system of interest in this thesis will be a Josephson Junction (JJ). Such a junction is formed by two weakly coupled superconductors. The weak coupling can be realized in a variety of ways. In the original work of Brian Josephson, after whom the junctions are named, the coupling was considered to be provided by a thin non-superconducting barrier placed between the superconductors. Later, it was realized that the system dynamics is very similar if the coupling is realized differently, e.g. via a point contact between superconductors or a constriction in a single superconducting layer (Dayem bridge). Originally, the name *Josephson junction* was reserved for tunneling junctions, while the other devices were referred to as *weak links*. In this thesis, we follow the current trends in the literature and use these two terms interchangeably.

The original prediction from 1962 was that if the barrier separating the superconductors is sufficiently thin, pairs of superconducting electrons (Cooper pairs) could tunnel right through it and thus sustain a supercurrent flowing through the junction. This prediction was experimentally confirmed a year later. Experiments show that for the tunneling to be possible, the thickness of the barrier is limited to several angstroms if it is a dielectric (Superconductor-Insulator-Superconductor, SIS junction), to several hundred angstroms if it is a semiconductor, and to several thousand angstroms if it is a normal metal (Superconductor-Normal metal-Superconductor, SNS junction).

A JJ, being a two-terminal electrical device, can be completely described by two expressions – one for the current, and one for the voltage. We will now show a simple derivation of these expressions using a two-level system, originally presented by Richard Feynman [13]. We will work within the framework of the Ginzburg-Landau phenomenological theory of superconductivity, according to which a single wavefunction can be used for a macroscopic number of electrons in a superconductor, which is said to be in a *macroscopic quantum state*. We will take the wavefunction to have the following form:

$$\psi = \sqrt{\rho} e^{i\varphi}, \quad (4.1)$$

where  $\varphi$  is the Ginzburg-Landau macroscopic phase, and  $\rho$  is the charge density. We will denote the two superconductors forming the junctions with the letters  $L$  and  $R$ . The state vectors of the two separate superconductors,  $|L\rangle$ , and  $|R\rangle$ , will be assumed to form a basis of our two-level system so that a general state can be written as

$$|\psi\rangle = \psi_R |R\rangle + \psi_L |L\rangle.$$

This time evolution of this state will be governed by the Schrödinger equation

$$i\hbar \frac{\partial |\psi\rangle}{\partial t} = \mathcal{H} |\psi\rangle, \quad (4.2)$$

with the following Hamiltonian:  $\mathcal{H} = \mathcal{H}_L + \mathcal{H}_R + \mathcal{H}_{\mathcal{T}}$ . Its first two terms are associated with the base states and have the following form:

$$\mathcal{H}_L = E_L |L\rangle \langle L|,$$

$$\mathcal{H}_R = E_R |R\rangle \langle R|,$$

where  $E_L$  and  $E_R$  are the ground state energies. The last term in the Hamiltonian is an interaction term (tunneling Hamiltonian) of the following form:

$$\mathcal{H}_{\mathcal{T}} = K(|L\rangle \langle R| + |R\rangle \langle L|),$$

with  $K$  measuring the strength of the coupling, which can depend on the junction structure, geometry, and material. By projecting Eq. (4.2) onto the base states we obtain

$$i\hbar \frac{\partial \psi_L}{\partial t} = E_L \psi_L + K \psi_R \quad (4.3)$$

$$i\hbar \frac{\partial \psi_R}{\partial t} = E_R \psi_R + K \psi_L. \quad (4.4)$$

From Gorkov's microscopic theory of superconductivity it can be shown that the ground state energies are  $E_L = 2\mu_L$  and  $E_R = 2\mu_R$ , where  $\mu_L$  and  $\mu_R$  are chemical potentials. If a voltage  $V$  is applied to the JJ, the chemical potentials are shifted by  $eV$  ( $e$  is the electron charge), so that  $E_L - E_R = 2eV$ . Taking this into consideration and choosing the zero energy level conveniently, we can write

$$i\hbar \frac{\partial \psi_L}{\partial t} = eV \psi_L + K \psi_R \quad (4.5)$$

$$i\hbar \frac{\partial \psi_R}{\partial t} = -eV \psi_R + K \psi_L. \quad (4.6)$$

By substituting the explicit expressions for the wavefunctions from (4.1), we get from the real parts

$$\begin{aligned} \frac{\partial \rho_L}{\partial t} &= \frac{2}{\hbar} K \sqrt{\rho_L \rho_R} \sin \phi \\ \frac{\partial \rho_R}{\partial t} &= -\frac{2}{\hbar} K \sqrt{\rho_L \rho_R} \sin \phi, \end{aligned} \quad (4.7)$$

and from the imaginary parts

$$\begin{aligned}\frac{\partial\phi_L}{\partial t} &= \frac{K}{\hbar}\sqrt{\frac{\rho_L}{\rho_R}}\cos\phi + \frac{eV}{\hbar} \\ \frac{\partial\phi_R}{\partial t} &= \frac{K}{\hbar}\sqrt{\frac{\rho_L}{\rho_R}}\cos\phi - \frac{eV}{\hbar},\end{aligned}\tag{4.8}$$

where  $\phi = \phi_L - \phi_R$ .

If we now define the pair current density  $I$  as  $\frac{\partial\rho_L}{\partial t} = -\frac{\partial\rho_R}{\partial t}$ , from Eq. (4.7) we get the first Josephson relation

$$I = I_c \sin\phi,\tag{4.9}$$

with  $I_c = 2K\rho_1/\hbar$ , and assuming  $\rho_1 = \rho_L = \rho_R = \text{const.}$  This assumption might seem contradictory, since we are assuming a value to be constant, and at the same time are working with its generally non-zero time derivative. It can be shown that this approach is consistent if the picture we are considering is extended with a current source which continuously replaces the tunneling pairs.

Under the above assumptions, from Eq. (4.8) we can also get the second Josephson relation

$$\frac{\partial\phi}{\partial t} = \frac{2eV}{\hbar}.\tag{4.10}$$

Eqs. (4.9) and (4.10) are the two constitutive relations for weak links, relating their macroscopic phase dynamics with the ordinary electrical current and voltage. It is interesting to use them to see what happens when different voltages are applied to the junction. First, if the external voltage is zero, Eq. (4.10) implies that the phase difference stays constant (not necessarily zero), and from Eq. (4.9) we see that a finite current can flow through the junction with zero voltage drop. The highest sustainable value of this supercurrent is  $I_c$  and is called the *critical current*. The process of supercurrent flow with zero voltage drop is called the *DC Josephson effect*. In contrast, the *AC Josephson effect* takes place when a constant voltage is applied, the result of which is an alternating current

$$I = I_c \sin\left(\phi_0 + \frac{2e}{\hbar}Vt\right).\tag{4.11}$$

The simple derivation presented above assumes a tunneling junction, for which a complete microscopic description can be given using the BCS theory of superconductivity and an appropriate tunneling Hamiltonian [2]. The microscopic theory yields a more complex expression for the current, in which Eq. (4.9) is extended by a  $\cos\phi$  term due to quasiparticle-Cooper pair interference and an additional term describing the quasiparticle tunneling current [29]. For our purposes, Eq. (4.9) will be a good enough approximation. Deviations from the simple sinusoidal relation between current and phase are explored in detail in the review paper by Golubov et al. [15]

The Josephson relations (4.9) and (4.10) are also known to be general enough to hold for many different kinds of weak links, including ones that do not have the simple three-layer geometry and where the coupling is not realized by a physical barrier made from a non-superconducting material.

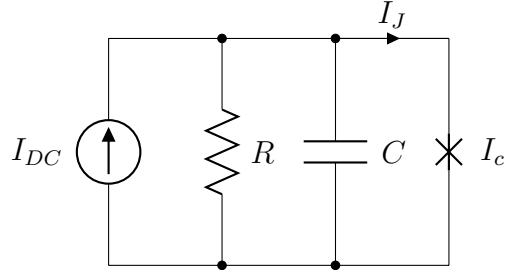


Figure 4.1: Stewart-McCumber model of a Josephson junction.  $I_J = I_c \sin \phi$

For the purpose of obtaining I-V characteristics, which is the main aim of this thesis, it is useful to work with a simplified, lumped circuit model of a JJ. In this model, the total current flowing through the junction is split into three components: the supercurrent of Cooper pairs, a normal current due to quasiparticle tunneling and a displacement current associated with the capacitance  $C$  of the junction [23]. The quasiparticles here refer to electron-like excitations that are created when thermal fluctuations break up some of the Cooper pairs in the superconductor [29]. Taking all three terms into account, the current balance equation can be written as

$$I = I_c \sin \phi + \frac{V}{R} + C \frac{dV}{dt}, \quad (4.12)$$

where  $R$  is the resistance associated with the junction and encountered by the quasiparticle current. The circuit described by this equation is formed by placing a resistor and a capacitor in parallel with the non-linear Josephson element, as shown in Figure 4.1. Using Eq. (4.10), Eq. (4.12) can be rewritten in terms of the phase difference  $\phi$  to read

$$I = I_c \sin \phi + \frac{\hbar}{2e} \frac{1}{R} \dot{\phi} + \frac{\hbar}{2e} C \ddot{\phi}. \quad (4.13)$$

This model of a JJ is known as the Resistively-Capacitively Shunted Junction (RCSJ) or the Stewart-McCumber model.

We will now want to extend it to include the effects of thermal noise. In order to do that, we add a Johnson-Nyquist noise current source to the current balance equation [41]

$$I = I_c \sin \phi + \frac{\hbar}{2e} \frac{1}{R} \dot{\phi} + \frac{\hbar}{2e} C \ddot{\phi} + \sqrt{\frac{2k_B T}{R}} \xi(t) \quad (4.14)$$

where the  $\langle \xi(t) \rangle = 0$ , and  $\langle \xi(t) \xi(s) \rangle = \delta(t - s)$ , and where the prefactor of  $\xi(t)$  is determined by the fluctuation-dissipation theorem, similarly to Eq. (2.9). This procedure

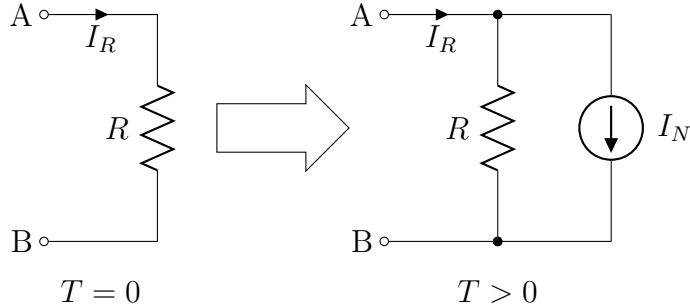


Figure 4.2: To include the effects of thermal noise, at finite temperatures a resistor is replaced by the parallel combination of a resistor and a noise current source.

of including noise into the dynamics of the system is based upon the idea of noise originating from the resistor, which is thus replaced by an equivalent circuit. Figure 4.2 presents this circuit in the Norton form.

The resulting Langevin description models thermal fluctuations but does not account for shot noise (high voltages) or the  $1/f$  noise, which are however only relevant for high voltages, and low frequencies, respectively [29].

Sometimes the description of the phase dynamics can be further simplified by using an *overdamped* model without the displacement current, which is valid if the second time derivative term in Eq. (4.14) can be neglected (i.e. if  $C \rightarrow 0$ ). This can be experimentally realized in point contacts, Dayem bridges, and metal barrier junctions, which have much lower capacitances (on the order of several picofarads) than tunneling structures with dielectric or semiconducting barriers [29]. Capacitances lower than 1 femtofarad are achievable with current fabrication technologies [31].

We now turn our attention to how the junctions can be externally driven. The driving current  $I$  in (4.14) will in general be assumed to consist of two components: a constant Direct Current (DC) bias  $I_{DC}$  and a sinusoidal Alternating Current (AC) component  $I_{AC} = a \cos(\omega t)$ . The DC bias is a normal current fed to the terminals of the device, while the AC drive is provided through microwave radiation shining onto the junction.

The RCSJ model is quite simple, and it is important to be aware of the limitations of its applicability. Since it completely neglects any spatial dependence of the phase difference  $\phi$  over the junction area, it can only be said to be valid for small area junctions (typical junction areas are smaller than  $1 \mu\text{m}^2$ ). More specifically, it can be shown that the spatial variations of  $\phi$  are small provided the width  $w$  and length  $l$  of the junction are smaller than the Josephson penetration depth  $\lambda_J = [2e\mu_0 I_c(s + 2\lambda_L)/\hbar]^{-1/2}$  where  $\mu_0$  is the permeability of free space, and  $\lambda_L$  is the London penetration depth for the superconductor used to build the junction [23] (see Figure 4.3).

Furthermore, for the model to be valid, the junction has to be operated at low frequencies

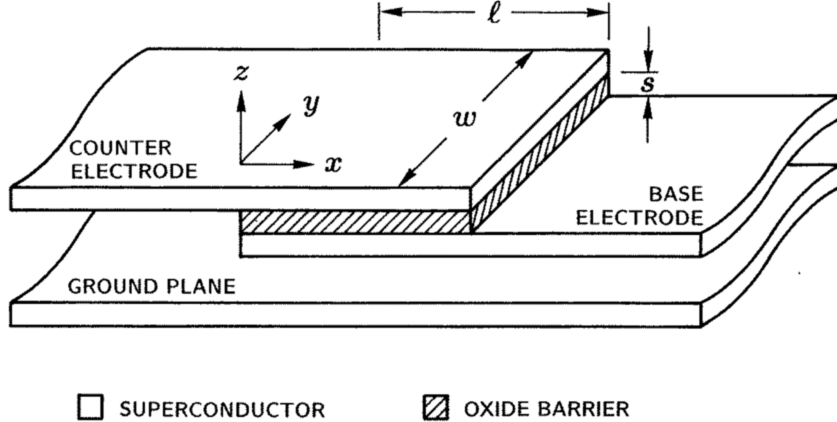


Figure 4.3: A schematic view of a Josephson tunnel junction with an oxide barrier. Picture reproduced from the review paper by Kautz [23].

of the AC drive, so that no significant amount of photon-assisted tunneling takes place. Photon-assisted tunneling is the name of a process in which photons from the external microwave radiation break up Cooper pairs, increasing the overall conductance of the junction.

After the discovery of the Josephson effect, weak links attracted considerable attention as perhaps the first devices in which the effects of a quantum quantity (the phase difference  $\phi$ ) could be observed directly in the macroscopic regime. JJs have subsequently found a multitude of practical applications: in the definition of a voltage standard [23], for the determination of the  $e/h$  constant [47], as building blocks of high speed integrated circuits (JJs can switch voltages within a few picoseconds and they exhibit low power consumption) and computer memory cells [29], in precise metrology using Superconducting Quantum Interference Devices (SQUIDs), as building blocks of qubits [24, 31], and recently also as models of neurons [10].

## 5 Single AC-driven Josephson junction

We begin our analysis of transport effects with the RCSJ model of a single Josephson junction subject to a DC bias and driven by an AC current

$$\left(\frac{\hbar}{2e}\right)C\ddot{\phi} + \left(\frac{\hbar}{2e}\right)\frac{1}{R}\dot{\phi} + I_c \sin \phi = I_d + I_a \cos(\Omega t) + \sqrt{\frac{2k_B T}{R}}\xi(t), \quad (5.1)$$

where  $R$ ,  $C$ ,  $\phi$ ,  $I_c$  and  $\xi(t)$  are the same as in (4.14), and  $I_d$  and  $I_a \cos(\Omega t)$  are the external DC and AC driving currents, respectively.

It is easily seen that Eq. (5.1) multiplied by  $\hbar/2e$  has the exact same form as the Langevin equation describing an inertial Brownian particle of mass  $M$

$$M\ddot{x} + \Gamma\dot{x} = -V'(x) + A \cos(\Omega t) + F + \sqrt{2\Gamma k_B T}\xi(t), \quad (5.2)$$

where  $V(x)$  is a spatially periodic, symmetric potential of period  $2\pi L$  and height  $2\Delta V$

$$V(x) = -\Delta V \cos(x/L). \quad (5.3)$$

The Brownian particle is subject to Stokes friction, the strength of which is determined by the parameter  $\Gamma$ , and to GWN  $\xi(t)$ , the strength of which follows from Eq. (2.9). The particle is driven by an oscillating force of angular frequency  $\Omega$  and amplitude  $A$ , as well as by a constant force  $F$  (which correspond to the AC and DC driving currents in the JJ model).

We now rescale Eq. (5.2) by introducing the dimensionless variables  $\hat{x} = x/L$ ,  $\hat{t} = t/\tau_0$ , where  $\tau_0 = L\sqrt{M/\Delta V}$ . Eq. (5.2) can now be rewritten as

$$\ddot{\hat{x}} + \gamma\dot{\hat{x}} = -\sin(\hat{x}) + a \cos(\omega\hat{t}) + f + \sqrt{2\gamma D_0}\xi(\hat{t}), \quad (5.4)$$

with  $f = FL/\Delta V$ ,  $a = AL/\Delta V$ ,  $\gamma = \tau_0\Gamma/M$ ,  $D_0 = k_B T/\Delta V$ , and  $\dot{\hat{x}} = d\hat{x}/d\hat{t}$ . From now on we shall omit the hat in the  $x$  and  $t$  variables, as we will be using rescaled variables exclusively unless noted otherwise. Eq. (5.4) is said to model a Brownian particle moving in a *rocked washboard potential*, and it has no known analytical solution.

### 5.1 Deterministic dynamics

The system described by Eq. (5.4) has a 5-dimensional parameter space  $\{\gamma, a, \omega, f, D_0\}$ . We start our analysis by looking at the dynamics of this system in the deterministic case

$D_0 = 0$ . Since  $f$  is the symmetry breaking parameter, we set it to a low value ( $f = 0.05$ ) and check how the average velocity of the particle  $\langle v \rangle$  depends on the remaining system parameters. If  $\langle v \rangle < 0$ , we will have detected some sort of anomalous transport, the exact nature of which (ANM, NNM) will have to be determined later. We limit our considerations to positive  $f$ , noting that the system (5.4) is symmetric around 0, so that  $\langle v \rangle(-f) = -\langle v \rangle(f)$ . We also note that Eq. (5.4) is invariant under changes of the sign of  $a$ .

This procedure leaves us with a 3-dimensional parameter space  $\{\gamma, a, \omega\}$ , the exploration of which is very tractable numerically with the currently available hardware. We performed scans of the following area of the parameter space:  $a \times \gamma \times \omega \in [0; 10] \times [0; 10] \times [0; 10]$  at a resolution of 100 points per dimension to determine the general behavior of the system.

Our scans reveal that negative mobility is not present for  $\omega > 2$  and  $\omega$  lower than about 0.01. This is in agreement with known approximate solutions of Eq. (5.4). In the limit of low frequencies, an adiabatic approximation is valid [8], while for high frequencies solutions can be approximated by Bessel functions [23]. We also observed that areas of negative mobility disappear for larger values of the friction coefficient (approximately  $\gamma > 1$ ). In the overdamped limit only thin strips of positive mobility remain.

We have therefore repeated the 3-dimensional parameter space scans, concentrating on the area  $a \times \gamma \times \omega \in [0; 10] \times [0; 1] \times [0.01; 2]$  where nontrivial mobility effects take place. On  $(\omega, a)$  cuts, the areas of negative mobility form a structure of thin strips, and a single larger „island” (see Figure 5.1).

On  $(\gamma, a)$  cuts, there is not net transport for  $a < 1$  and low driving frequencies  $\omega$ . The areas of non-zero mobility also have a striped structure (see Figure 5.1 and Figure 5.2). Increasing  $\omega$  causes the strips to become wider (subsequently, there is less of them in the area over which the scans were performed). At  $\omega = 1$  the strips are no longer visible, and instead they now appear as „islands” of non-zero mobility.

The scans also allowed us to determine the optimal values for the presence of negative mobility:  $\gamma \approx 0.19$ , and  $\omega \approx 0.6$  (see Figure 5.3).

We continue analyzing the system on  $(\gamma, a)$  cuts at  $\omega = 0.6$ , where it is easiest to explain the changes in its dynamics for different values of  $f$ . When trying to find the origin of the negative mobility effects, it is instructive to look at the behavior of the average modulus of the velocity  $\langle |v| \rangle$  at  $f = 0$ . While the average velocity  $\langle v \rangle$  is expected to vanish everywhere when  $f = 0$ , the same is not necessarily true for the average modulus of the velocity. In Figure 5.2(a) it is evident that there exist areas of the parameter space where attractors for both positive and negative velocity coexist. At  $f = 0$ , their basins of attraction are of the same size, so that there is no net motion. When the symmetry of the system is broken by a non-zero  $f$ , the regions of positive and negative velocity start to deform and diverge, and in some areas only the negative velocity prevails (see

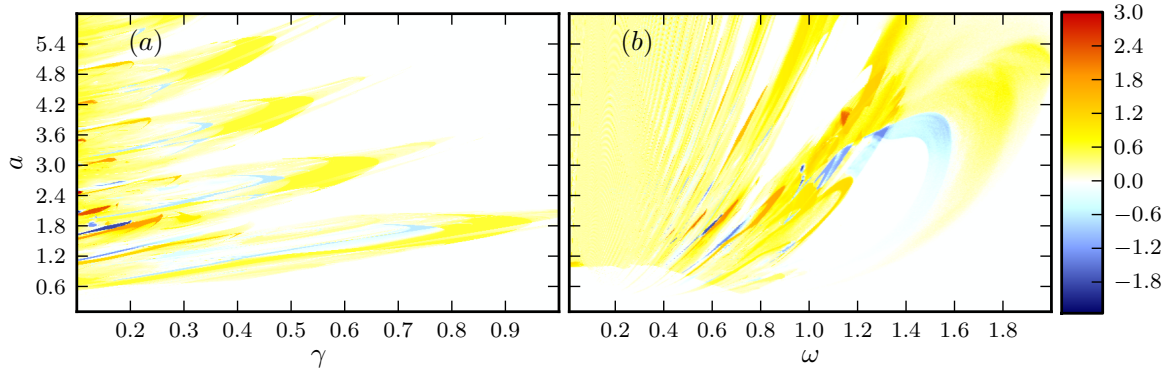


Figure 5.1:  $\langle v \rangle$  at  $D_0 = 0$ ,  $f = 0.05$ . Panel (a):  $\omega = 0.6$ , panel (b):  $\gamma = 0.19$ .

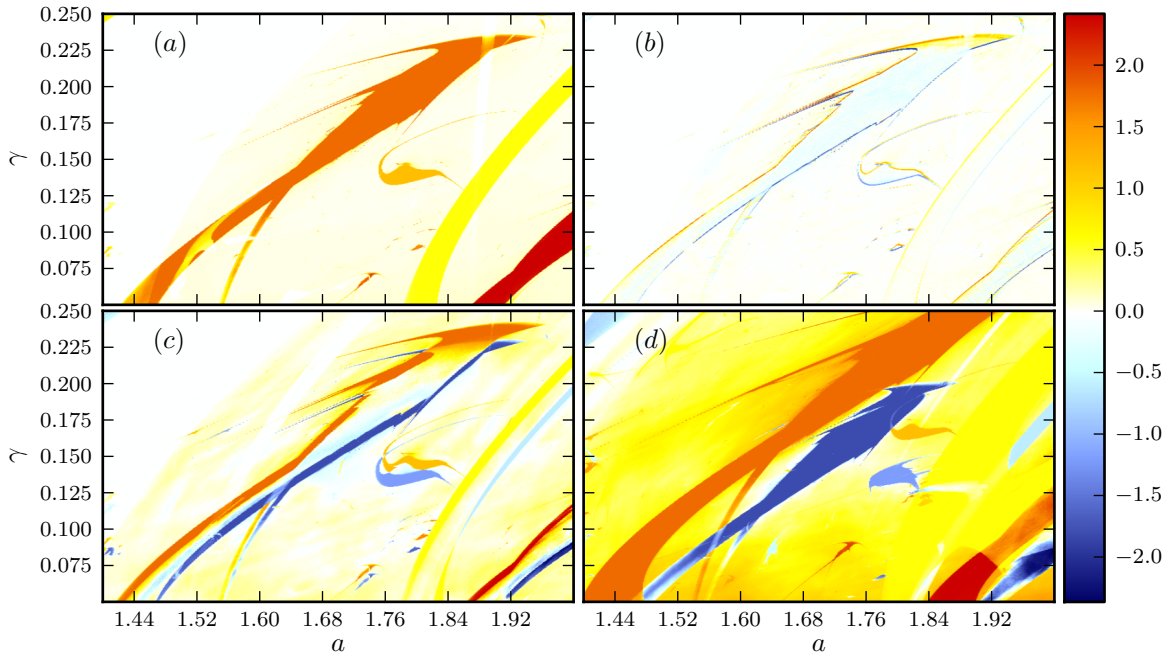


Figure 5.2: Average velocity for different values of the bias force  $f$ , with  $D_0 = 0$ ,  $\omega = 0.6$ .  
 Panel (a):  $\langle |v| \rangle$ ,  $f = 0.0$ , panels (b)-(d):  $\langle v \rangle$  at  $f = 0.001, 0.01, 0.06$ , respectively.

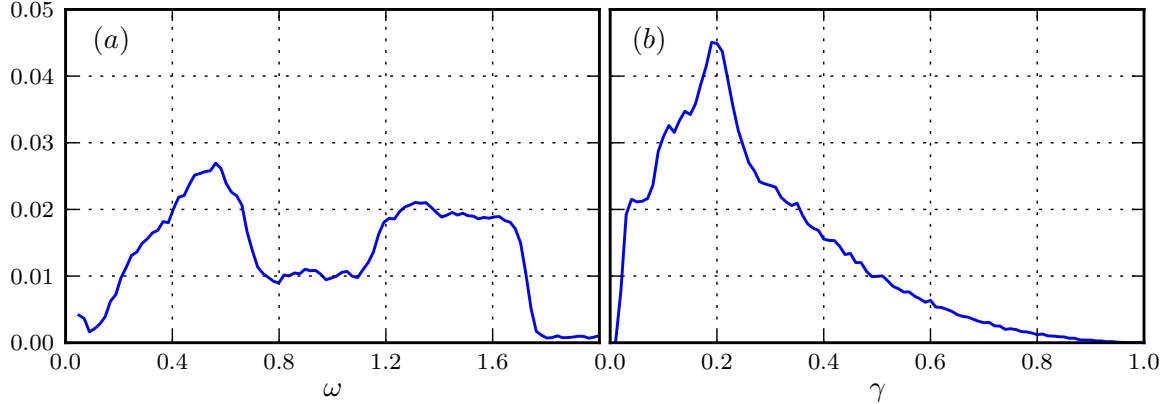


Figure 5.3: Fraction of negative mobility area in the analyzed parameter space,  $f = 0.05$ ,  $D_0 = 0$ . Panel (a):  $\gamma \in (0; 1)$ ,  $a \in (0; 10)$ . Panel (b):  $\omega \in (0; 2)$ ,  $a \in (0; 10)$ .

Figure 5.2(b)-(d)). The velocity on the plots is averaged over initial conditions, which corresponds to a weighted average over attractors, with weights proportional to the size of the basins of attraction.

Looking at the plots we see that the general tendency for the regions of positive velocity is to move up towards higher values of  $\gamma$  as  $f$  is increased, while the regions of negative velocity exhibit an opposite tendency and move towards lower values of  $\gamma$ . This can be understood on the grounds of the following intuitive and non-rigorous argument, based on the idea of constant dissipation. Dissipation is generally higher for larger values of  $\gamma$ . We now take any point at the border of the area of non-zero mobility in Figure 5.2(a), and consider what happens when a small positive bias force  $f$  is applied. The solution with positive velocity will gain energy from the bias, and thus dissipate less. In order to keep its previous rate of dissipation, the solution will then move towards higher values of  $\gamma$ . In contrast, the negative velocity solution will dissipate more in the presence of a positive  $f$ , so it will be able to move towards lower values of  $\gamma$  while keeping the overall dissipation constant.

The underlying dynamics of the system (5.4) is very rich, and has been studied for quite some time. This is because Eq. (5.4) models a large variety of physical systems, e.g. rotating dipoles in external fields, superionic conductors, charge density waves, fluxons in semiconductors, and pendulums under torque. The model has also been used to study phase locking, intracellular transport in biological systems and neural activity [23, 46].

Depending on the system parameters, the solutions of (5.4) in the noiseless case can be periodic (phase locked), quasiperiodic and chaotic. Chaotic motion in this system was studied in both the noiseless and the noisy case by Iansiti et al. [20]. In Figure 5.4 the chaotic motion of the particle is shown. In the Poincaré section, a strange attractor is visible, a well-known indication of chaotic dynamics [42].

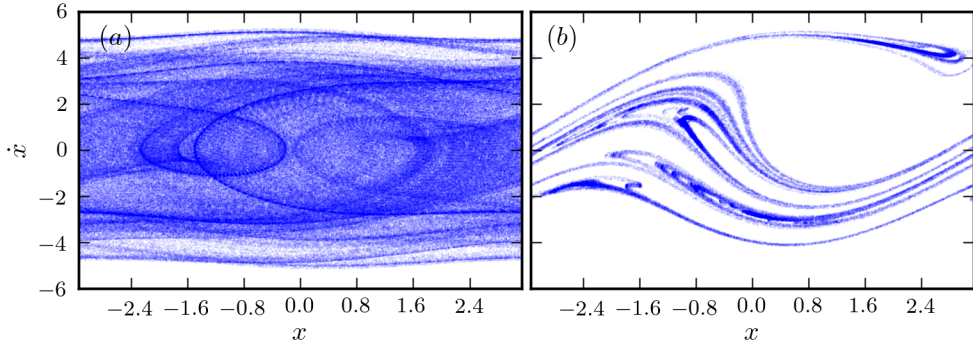


Figure 5.4: Chaotic motion of a particle in the rocking washboard potential. Parameters are:  $f = 0.01$ ,  $\omega = 0.6$ ,  $\gamma = 0.14$ ,  $a = 1.84$ ,  $D_0 = 0$ . Initial conditions are  $x = 0$ ,  $\dot{x} = 0$ . Panel (a): phase portrait, panel (b): Poincaré section at the beginning of the driving period. 100000 driving periods are plotted.

A solution is said to be *periodic* if  $x$  advances by  $2\pi k$  over  $m$  AC driving cycles (see Figure 5.5). In this case, the *winding number* can be defined as  $r = k/m$ . If this number is irrational, the solution is said to be *quasiperiodic*.

The solutions can also be divided into locked and running ones. In locked states, motion of the particle is confined to a limited number of spatial periods. In contrast, in running states, which are crucial for transport, the motion is unbounded in space.

## 5.2 Impact of noise

Intuitively, one can expect that the introduction of noise to the system will perturb its deterministic dynamics. This intuition is confirmed by inspection of Figure 5.6, where the average velocity  $\langle v \rangle$  is plotted for different values of the noise intensity  $D_0$ . We observe that larger areas of negative mobility are relatively stable with respect to increasing temperature, while the smaller areas disappear more quickly. For high enough temperatures, negative mobility disappears completely.

Temperature has a smoothing effect on the plots, erasing the finer details of the structures visible in the deterministic case (cf. panels (a) and (b) in Figure 5.6). This is to be expected, because the introduction of noise causes random transitions between coexisting basins of attraction (see Figure 5.7).

A perhaps surprising finding is that negative mobility can be induced and strengthened by noise. Careful inspection of Figure 5.6 reveals areas of the parameter space where the average velocity  $\langle v \rangle$  is 0 in the deterministic case, but becomes negative upon the introduction of noise (see Figure 5.8 and Figure 5.9). Furthermore, it is possible to

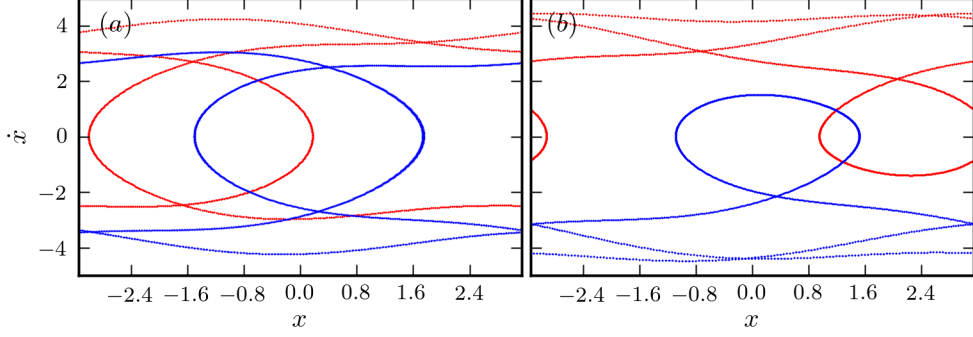


Figure 5.5: Phase portraits of phase locked motion of a particle in the rocking washboard potential. Red orbits represent motion in the positive direction, and blue orbits in the negative direction. Common parameters are  $D_0 = 0$ ,  $f = 0.01$ ,  $\omega = 0.6$ . Panel (a):  $a = 1.937$ ,  $\gamma = 0.18$  (red orbit),  $\gamma = 0.16$  (blue orbit),  $r = 1$ . Panel (b):  $a = 1.5868$ ,  $\gamma = 0.1234$  (red orbit),  $\gamma = 0.1119$  (blue orbit),  $r = 3$ .

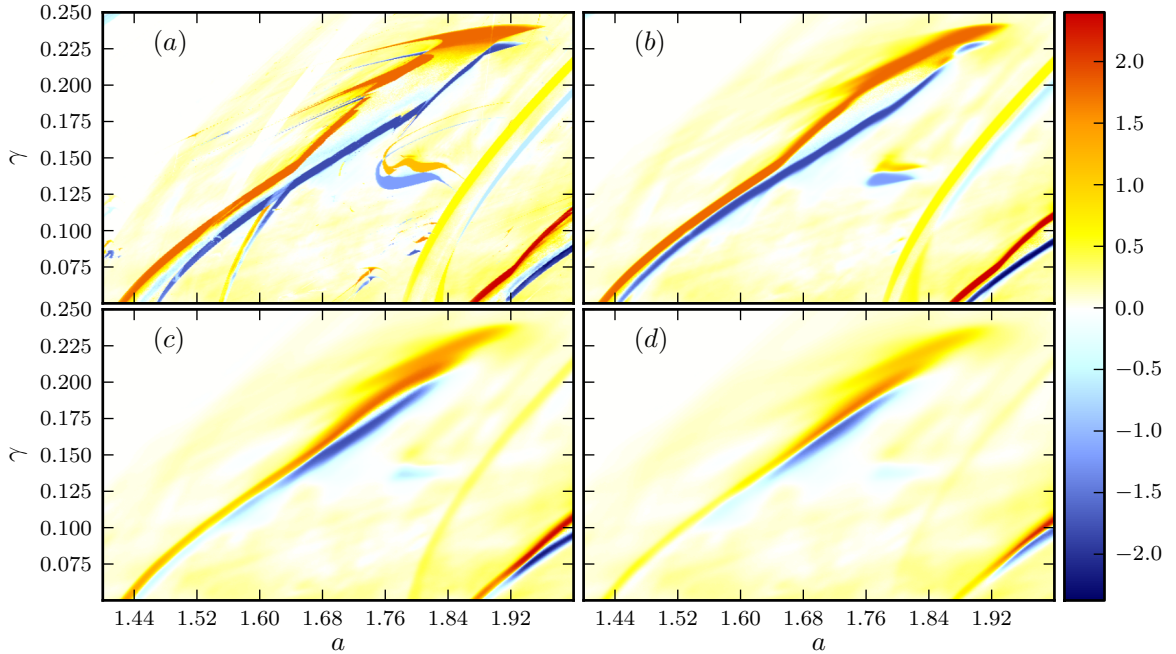


Figure 5.6: Average velocity  $\langle v \rangle$  at  $f = 0.01$ ,  $\omega = 0.6$  and different temperatures.  $D_0 = 0.0, 0.0001, 0.0005, 0.001$  for panels (a)-(d), respectively.

find parameter values, where deterministic ANM is strengthened (see Figure 5.10), and where thermal fluctuations turn positive mobility into a negative one (see Figure 5.11). The most usual and least unexpected effect, in which noise diminishes the strength of

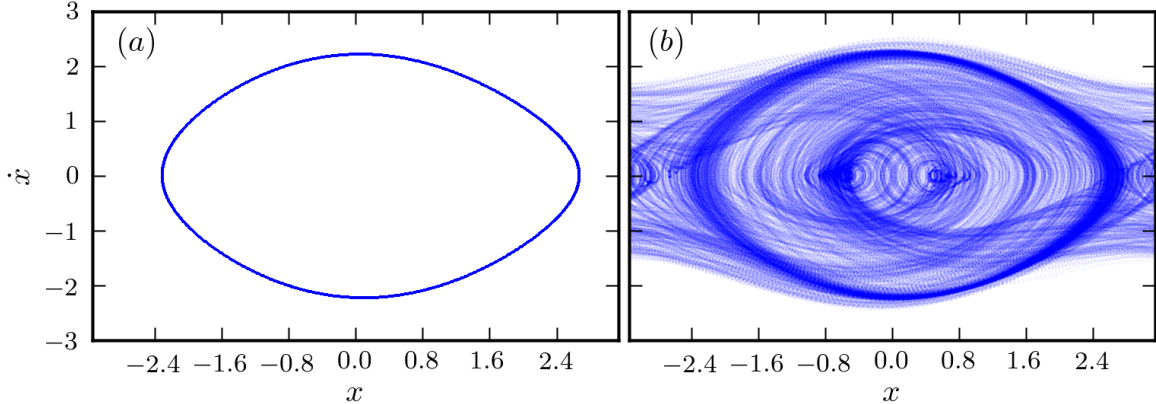


Figure 5.7: Phase portrait of the system for  $\omega = 0.78$ ,  $a = 0.668$ ,  $\gamma = 0.143$ ,  $f = 0.015$ . Panel (a) represents the deterministic system ( $D_0 = 0.0$ ) and only a single stable limit cycle is visible. Panel (b) on the other hand represents the noisy system at  $D_0 = 0.001$ , where thermal fluctuations induce jumps between the stable limit cycle and multiple unstable (periodic) orbits.

deterministic ANM is presented in Figure 5.12. The more common NDM and NNM are also found in many parameter regimes (see Figure 5.13 for an example).

At first glance, it might appear that the presence of negative mobility effects violates the laws of physics. We have already discussed why this effect does *not* violate the second law of thermodynamics (see Chapter 2). Another law that seems to be violated by negative mobility is Newton's second law of motion. If the force  $F$  is increased from 0 to a finite value, we would expect an acceleration in the direction of the force and also an average velocity of the same sign as that of the force. This argument is however inconclusive here due to the nonlinearity of the equation of motion ensured by the spatial potential  $V(x)$  – the effects of the forces present when  $F = 0$  and of the external bias force  $F$  cannot simply be superimposed, as would be the case if the system were linear.

One might also wonder whether the system (5.4) is minimal for negative mobility effects to appear. This is indeed the case, which can be shown through the following simple argument originally given by Speer et al. [46]. Consider a non-inertial system of the following form:

$$\dot{x} = h(x, t) + F + g(x, t)\xi(t) \quad (5.5)$$

Under the assumption of ergodicity, the average velocity  $\langle v \rangle$  can be defined by Eq. (2.15) and it is then independent of the initial conditions and the realizations of the noise  $\xi(t)$ . We can now consider two solutions to Eq. (5.5),  $x_1(t)$  and  $x_2(t)$ , with identical realization of the noise and identical seeds  $x_1(0) = x_2(0)$ , but with  $F_1 > F_2$ . If at some time  $t$  the solutions cross, that is  $x_1(t) = x_2(t)$ , it would imply  $\dot{x}_1(t) - \dot{x}_2(t) = F_1 - F_2 > 0$ . We could then conclude that  $x_1(t) \geq x_2(t)$  for all  $t$  and thus by Eq. (2.15) also  $\langle v_1 \rangle \geq \langle v_2 \rangle$ .

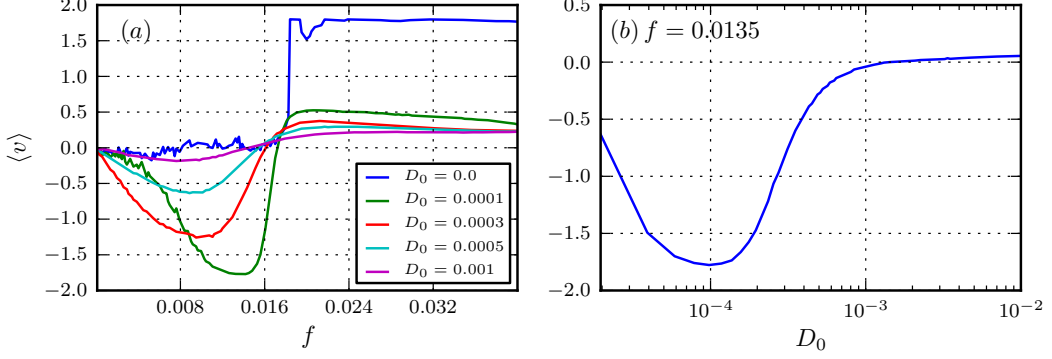


Figure 5.8: Constructive influence of thermal fluctuations on the ANM effect.  $\omega = 0.6$ ,  $a = 1.62151$ ,  $\gamma = 0.13$ .

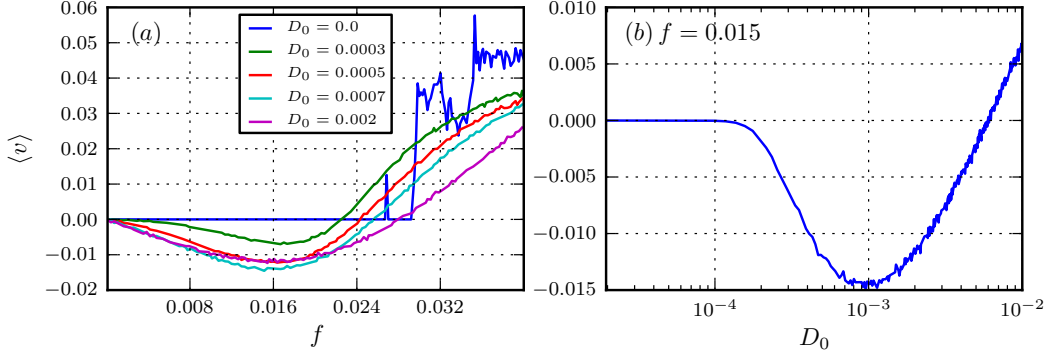


Figure 5.9: Constructive influence of thermal fluctuations on the ANM effect.  $\omega = 4.9/2\pi$ ,  $a = 4.2/2\pi$ ,  $\gamma = 0.9/2\pi$ . Parameters correspond to those reported by Machura et al. [30]

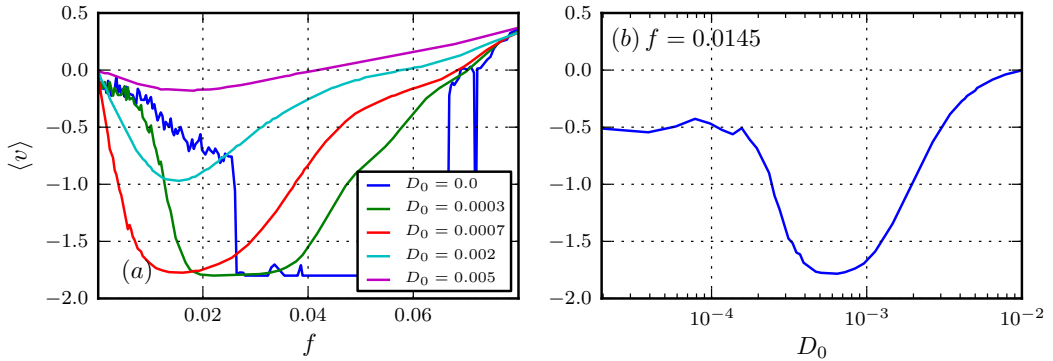


Figure 5.10: Thermal fluctuations increasing the strength of the ANM effect for low values of  $f$ .  $\omega = 0.6$ ,  $a = 1.721042$ ,  $\gamma = 0.165832$ .

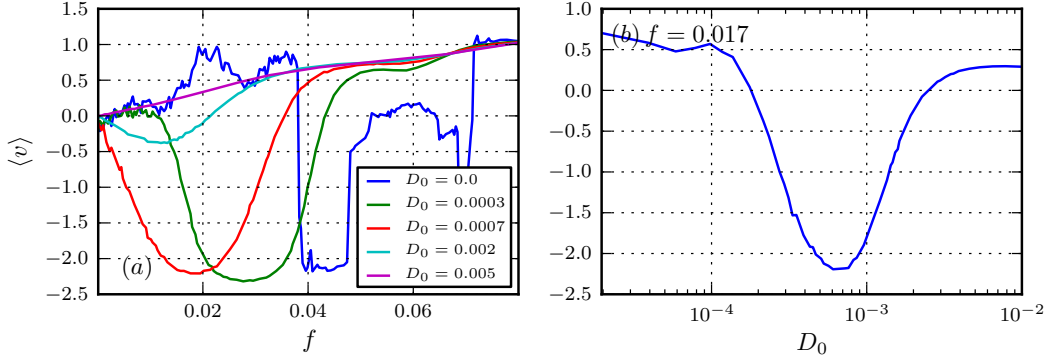


Figure 5.11: Thermal fluctuations reversing the mobility of the particle.  $\omega = 0.6$ ,  $a = 1.997595$ ,  $\gamma = 0.098096$ .

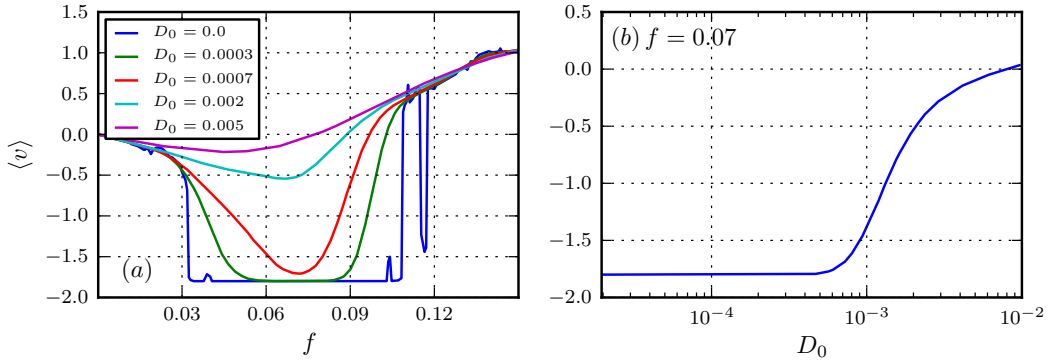


Figure 5.12: Destructive influence of thermal fluctuations on the ANM effect.  $\omega = 0.6$ ,  $a = 1.725852$ ,  $\gamma = 0.1502$ .

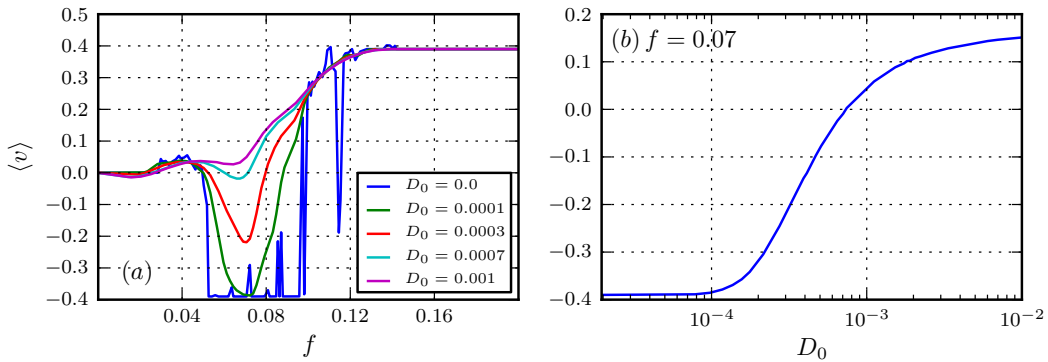


Figure 5.13: Influence of thermal fluctuations on the NDM and NNM effects.  $\omega = 0.78$ ,  $a = 0.668$ ,  $\gamma = 0.143$ .

We can conclude that the average velocity  $\langle v \rangle$  is a monotonically increasing function of  $F$ , which precludes the presence of any negative mobility effects. This argument is valid under the assumption continuous ergodic dynamics.

Next, we check whether the damping term  $\gamma \dot{x}$  is necessary for negative mobility. If we were to omit it, it would be equivalent to making  $\gamma \rightarrow 0$  while keeping  $\gamma T = \text{const}$ , which would imply that the system is coupled to an infinitely hot bath. In this case, the influence of the spatial potential  $V(x)$  (and in fact all other deterministic forces) would become negligible. That in turn would invalidate our argument about not violating Newton's second law of motion. We can thus conclude that no negative mobility would be present in this case.

By the arguments presented above, the system (5.4) is minimal for the presence of negative mobility effects.

### 5.3 Interpretation in the Stewart-McCumber model

In order to interpret the results within the framework of the RCSJ model, we need to again rescale all quantities. To do that, we use the Josephson plasma frequency

$$\omega_p = \sqrt{\frac{2eI_c}{\hbar C}}, \quad (5.6)$$

the relation between our dimensionless friction  $\gamma$  and the quantities used in the RCSJ model

$$\gamma = \frac{1}{RC\omega_p}, \quad (5.7)$$

and the following expression linking the dimensionless temperature  $D_0$  with the physical temperature  $T$ :

$$T = \frac{E_J}{k_B} D_0, \quad (5.8)$$

where  $E_J = \hbar I_c / 2e$  is the Josephson coupling energy.

This allows us to write the following relations:

$$V = \frac{\hbar\omega_p}{2e} \langle v \rangle, \quad \Omega = \omega\omega_p, \quad I_{AC} = I_c a, \quad I_{DC} = I_c f. \quad (5.9)$$

To illustrate the whole procedure, we will follow it step by step for the system parameters from Figure 5.8, that is  $\omega = 0.6$ ,  $a = 1.62151$ ,  $\gamma = 0.13$ ,  $D_0 = 0.0003$ , and  $f = 0.01$ . The Absolute Negative Mobility (ANM) effect numerically predicted for these parameters should be visible in the I-V characteristic of an appropriately prepared Josephson junction, in the form of absolute negative conductance (negative voltage causes positive current flow).

The rescaling procedure is as follows:

1. Set the desired temperature  $T$ , e.g. 10 K.
2. Use Eq. (5.8) to calculate  $E_J$ , and thus the critical current  $I_c \approx 1.398 \text{ mA}$ .
3. Calculate the driving amplitude and the bias amplitude using Eq. (5.9):  $I_{AC} = 2.268 \text{ mA}$ ,  $I_{DC} \approx 0.014 \text{ mA}$ .
4. Set the frequency of the incident microwave radiation, e.g.  $\Omega = 100 \text{ GHz}$ .
5. Calculate the plasma frequency using Eq. (5.9),  $\omega_p = 167 \text{ GHz}$ .
6. Calculate the voltage using Eq. (5.9):  $V \approx -0.0658 \text{ mV}$ .
7. Check whether we are in the semiclassical regime, which is implicitly assumed in the RCSJ model. Make sure the following inequalities are obeyed:

$$\hbar\omega_p \ll E_J, \quad \hbar\omega_p \ll k_B T. \quad (5.10)$$

8. Use Eq. (5.6) to calculate the capacitance of the junction  $C \approx 152.966 \text{ pF}$ .
9. Use Eq. (5.7) to calculate the resistance of the junction  $R \approx 0.301 \Omega$ .

## 5.4 Note on previous work

The effect of ANM in the system described by Eq. (5.4) was first reported in 2007 in the work of Machura et al. [30]. The analysis presented there was extended with further details in a few subsequent papers [27, 46]. Our findings presented in this chapter fully agree with the observations presented in the above-mentioned papers. Within a year of the initial discovery, the presence of ANM was confirmed experimentally by Nagel et al. in an experiment involving the determination of I-V characteristics of microwave-driven Josephson junctions [34]. ANM has also been determined to exist in the system in the presence of colored noise [28].

Before the discovery of ANM in (5.4), the effects of negative mobility have been known to exist in more complex systems, such as GaAs quantum wells [19], Brownian particles in 2D tailored structures [12], and Brownian particles in tilted symmetric sawtooth potentials [16]. It is fascinating that the presence of anomalous mobility in the mathematically minimal system (5.4) has escaped the attention of researchers for so long. It serves to demonstrate that surprising effects still remain to be discovered in simple dynamical systems.

## 6 Two overdamped AC-driven Josephson junctions

Having analyzed the phase dynamics of a single Josephson Junction (JJ), we now proceed to a slightly more complex system composed of two coupled, overdamped JJs. Such a system subject to an external AC driving has a three-dimensional phase space, and is thus mathematically minimal with regard to chaotic dynamics. The system we will be working with was analyzed in the noiseless case by Nerenberg et al. [11, 36], who detected the phenomenon of voltage locking between the two junctions. This numerical and theoretical prediction was subsequently confirmed experimentally [22]. Their work was then extended to an analysis of deterministic chaos in the phase dynamics [37], the presence of which was later experimentally confirmed by the means of an analog simulation [4].

In the following two sections we consider two different coupling mechanisms and derive the equations of motion of the junction phases for both of them. Both types of coupling described here, as well as several other interaction mechanisms between JJs are discussed in the review paper by Hansen and Lindelof [17].

## 6.1 Resistive shunt coupling

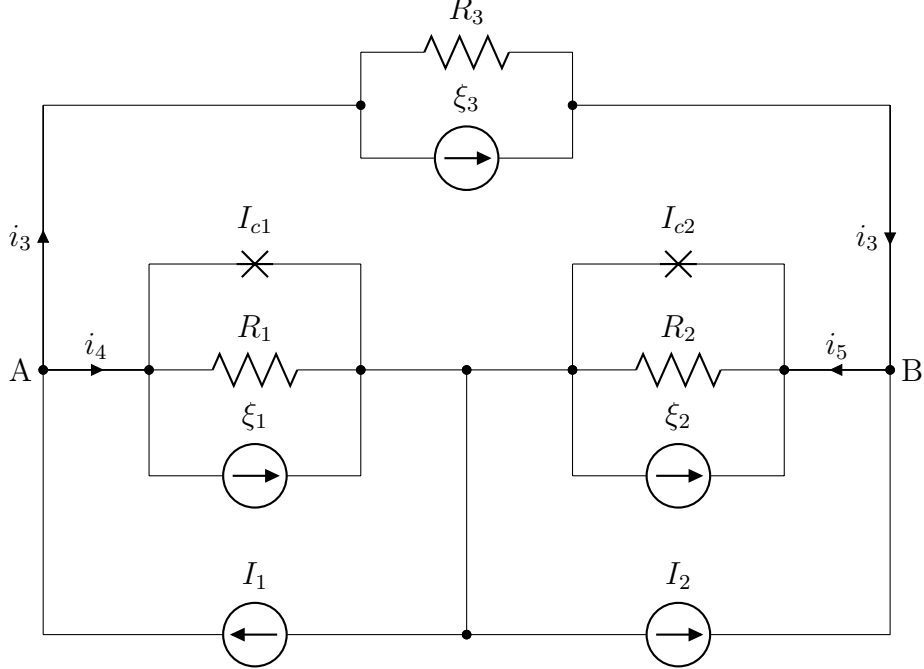


Figure 6.1: Two overdamped Josephson junctions shunted by an external resistance  $R_3$ .

We begin the derivation by considering the noiseless variant of the system of two JJs shunted by an external resistance (see Figure 6.1). In the noiseless case the noise current sources  $\xi_1(t)$ ,  $\xi_2(t)$  and  $\xi_3(t)$  are identically zero.

Kirchhoff's current law for the nodes  $A$  and  $B$  implies

$$i_4 = I_1 - i_3 \quad (6.1a)$$

$$i_5 = I_2 + i_3. \quad (6.1b)$$

Using the Kirchhoff's voltage law and Eq. (4.12) in the overdamped ( $C \rightarrow 0$ ) and noiseless case ( $\xi(t) = 0$ ) we can write

$$i_3 R_3 - (i_4 - I_{c1} \sin \phi_1) R_1 + (i_5 - I_{c2} \sin \phi_2) R_2 = 0. \quad (6.2)$$

Combining this with Eq. (6.1) and regrouping the terms we obtain

$$i_3 (R_1 + R_2 + R_3) - (I_1 - I_{c1} \sin \phi_1) R_1 + (I_2 - I_{c2} \sin \phi_2) R_2 = 0, \quad (6.3)$$

from which we get an expression for the deterministic current  $i_3$

$$i_3 = \frac{i_{h1} R_1 - i_{h2} R_2}{R_1 + R_2 + R_3}, \quad (6.4)$$

where for clarity we introduced the new notation  $i_{hi} = I_i - I_{ci} \sin \phi_i$  for the current terms in the current-voltage equation of the  $i$ -th Josephson junction.

We can now write the equations for voltage across both of the junctions:

$$\begin{aligned}\frac{V_1}{R_1} &= \frac{1}{R_1} \frac{\hbar}{2e} \frac{d\phi_1}{dt} = i_{h1} - i_3 \\ \frac{V_2}{R_2} &= \frac{1}{R_2} \frac{\hbar}{2e} \frac{d\phi_2}{dt} = i_{h2} + i_3.\end{aligned}$$

Using Eq. (6.4) and regrouping the terms:

$$\left( \sum_{i=1}^3 R_i \right) \frac{\hbar}{2e} \frac{d\phi_1}{dt} = i_{h1} R_1 (R_2 + R_3) + i_{h2} R_2 R_1 \quad (6.5a)$$

$$\left( \sum_{i=1}^3 R_i \right) \frac{\hbar}{2e} \frac{d\phi_2}{dt} = i_{h1} R_1 R_2 + i_{h2} R_2 (R_1 + R_3). \quad (6.5b)$$

We can now define the characteristic voltage as

$$V_0 = \bar{I}_c \frac{R_1 (R_2 + R_3)}{R_1 + R_2 + R_3}, \quad (6.6)$$

with  $\bar{I}_c = \frac{I_{c1} + I_{c2}}{2}$ . Normalizing the time with  $\hat{t} = t \frac{2eV_0}{\hbar}$  and introducing the coupling coefficients

$$\begin{aligned}\alpha &= \frac{R_2}{R_2 + R_3} \\ \beta &= 1 + \frac{R_3}{R_1},\end{aligned}$$

we obtain from Eq. (6.5)

$$\frac{d\phi_1}{d\hat{t}} = \hat{i}_{h1} + \hat{i}_{h2}\alpha \quad (6.7a)$$

$$\frac{d\phi_2}{d\hat{t}} = \hat{i}_{h1}\alpha + \hat{i}_{h2}\alpha\beta, \quad (6.7b)$$

where the normalized currents are now expressed in units of  $\bar{I}_c$ . In all subsequent equations, the hat signs will be dropped as we shall from now on use normalized quantities exclusively unless noted otherwise.

With the assumed normalization scheme, the currents take values from the range  $(0; 2)$  and satisfy the relationship  $I_{c1} + I_{c2} = 2$ . The coupling constants take values  $\alpha \in (0; 1)$

and  $\beta \in (1; \infty)$ . In the limiting case of infinitely large shunting resistance  $R_3 \rightarrow \infty$ , the coupling constants take the values  $\alpha = 0$ ,  $\alpha\beta = R_2/R_1$  and the system of equations (6.7) becomes uncoupled.

We now wish to obtain an explicit form of the equations of motion Eq. (6.7) in the noisy case. We do this by including the noise sources  $\xi_i(t)$  into the circuit analysis. The expression for  $i_3$  (unnormalized) becomes

$$i_3 = \frac{i_{h1}R_1 - i_{h2}R_2 - L_1(t) + L_2(t) + L_3(t)}{R_1 + R_2 + R_3}, \quad (6.8)$$

where  $L_i(t) = \sqrt{2k_B T R_i} \xi_i(t)$  represents the  $i$ -th noise voltage. The expressions for voltage across the junctions now read

$$\begin{aligned} \frac{1}{R_1} \frac{\hbar}{2e} \frac{d\phi_1}{dt} &= i_{h1} - i_3 - \sqrt{\frac{2k_B T}{R_1}} \xi_1(t) \\ \frac{1}{R_2} \frac{\hbar}{2e} \frac{d\phi_2}{dt} &= i_{h2} + i_3 - \sqrt{\frac{2k_B T}{R_2}} \xi_2(t). \end{aligned}$$

The analog of Eq. (6.5) thus becomes

$$\begin{aligned} \left( \sum_{i=1}^3 R_i \right) \frac{\hbar}{2e} \frac{d\phi_1}{dt} &= i_{h1} R_1 (R_2 + R_3) + i_{h2} R_2 R_1 - L_{s1}(t) \\ \left( \sum_{i=1}^3 R_i \right) \frac{\hbar}{2e} \frac{d\phi_2}{dt} &= i_{h1} R_1 R_2 + i_{h2} R_2 (R_1 + R_3) - L_{s2}(t), \end{aligned}$$

with

$$\begin{aligned} L_{s1}(t) &= (R_2 + R_3) L_1(t) + R_1 (L_2(t) + L_3(t)) \\ L_{s2}(t) &= R_2 (L_1(t) - L_3(t)) + (R_1 + R_3) L_2(t). \end{aligned}$$

Using the previously described time normalization and coupling constants, and introducing the dimensionless noise strength  $D_1 = \frac{4k_B T e V_0}{\hbar I_c^2 R_3}$ , we obtain

$$\begin{aligned} \frac{d\phi_1}{dt} &= I_1 - I_{c1} \sin \phi_1 - \sqrt{D_1 \frac{R_3}{R_1}} \xi_1(t) \\ &\quad + \alpha \left( I_2 - I_{c2} \sin \phi_2 - \sqrt{D_1 \frac{R_3}{R_2}} \xi_2(t) \right) - \frac{R_3}{R_2 + R_3} \sqrt{D_1} \xi_3(t) \\ \frac{d\phi_2}{dt} &= \alpha \left( I_1 - I_{c1} \sin \phi_1 - \sqrt{D_1 \frac{R_3}{R_1}} \xi_1(t) \right) \\ &\quad + \alpha \beta \left( I_2 - I_{c2} \sin \phi_2 - \sqrt{D_1 \frac{R_3}{R_2}} \xi_2(t) \right) + \frac{R_2 R_3}{R_1 (R_2 + R_3)} \sqrt{D_1} \xi_3(t). \end{aligned}$$

If we now notice that  $\frac{R_3}{R_1} = (\beta - 1)$ ,  $\frac{R_3}{R_2} = \frac{1 - \alpha}{\alpha}$ ,  $\frac{R_3}{R_2 + R_3} = 1 - \alpha$  and  $\frac{R_2 R_3}{R_1 (R_2 + R_3)} = \alpha(\beta - 1)$ , we can rewrite these equations as

$$\begin{aligned}\frac{d\phi_1}{dt} &= I_1 - I_{c1} \sin \phi_1 - \sqrt{D_1(\beta - 1)} \xi_1(t) \\ &\quad + \alpha \left( I_2 - I_{c2} \sin \phi_2 - \sqrt{D_1 \frac{1 - \alpha}{\alpha}} \xi_2(t) \right) - (1 - \alpha) \sqrt{D_1} \xi_3(t) \\ \frac{d\phi_2}{dt} &= \alpha \left( I_1 - I_{c1} \sin \phi_1 - \sqrt{D_1(\beta - 1)} \xi_1(t) \right) \\ &\quad + \alpha \beta \left( I_2 - I_{c2} \sin \phi_2 - \sqrt{D_1 \frac{1 - \alpha}{\alpha}} \xi_2(t) \right) + \alpha(\beta - 1) \sqrt{D_1} \xi_3(t).\end{aligned}$$

They can be further simplified by utilizing the noise addition rule (2.11):

$$\frac{d\phi_1}{dt} = I_1 - I_{c1} \sin \phi_1 + \alpha(I_2 - I_{c2} \sin \phi_2) + \sqrt{(\beta - \alpha) D_1} \xi'(t) \quad (6.9a)$$

$$\frac{d\phi_2}{dt} = \alpha(I_1 - I_{c1} \sin \phi_1) + \alpha \beta(I_2 - I_{c2} \sin \phi_2) + \sqrt{(\beta - \alpha) \alpha \beta D_1} \xi''(t), \quad (6.9b)$$

where  $\xi'(t)$  and  $\xi''(t)$  are new zero-mean,  $\delta$ -correlated noise terms.

We can now make one final simplification by noting that  $V_0/\bar{I}_c R_3 = 1/(\beta - \alpha)$ . This allows us to define a new dimensionless noise strength  $D_0 = \frac{4e k_B T}{\hbar \bar{I}_c} = D_1(\beta - \alpha)$ , and rewrite Eq. (6.9) in the following form:

$$\frac{d\phi_1}{dt} = I_1 - I_{c1} \sin \phi_1 + \alpha(I_2 - I_{c2} \sin \phi_2) + \sqrt{D_0} \xi'(t) \quad (6.10a)$$

$$\frac{d\phi_2}{dt} = \alpha(I_1 - I_{c1} \sin \phi_1) + \alpha \beta(I_2 - I_{c2} \sin \phi_2) + \sqrt{\alpha \beta D_0} \xi''(t). \quad (6.10b)$$

We will now want to add an AC current driving the junctions. This can be done by substituting:  $I_i \rightarrow I_i + a_i \cos(\omega t)$  (for simplicity we assume that the frequency of the driving is the same for both junctions). Eqs. (6.10) can then be rewritten as

$$\frac{d\phi_1}{dt} = I_1 - I_{c1} \sin \phi_1 + \alpha(I_2 - I_{c2} \sin \phi_2) + \sqrt{D_0} \xi'(t) + b_1 \cos(\omega t) \quad (6.11a)$$

$$\frac{d\phi_2}{dt} = \alpha(I_1 - I_{c1} \sin \phi_1) + \alpha \beta(I_2 - I_{c2} \sin \phi_2) + \sqrt{\alpha \beta D_0} \xi''(t) + b_2 \cos(\omega t), \quad (6.11b)$$

where  $b_1 = a_1 + \alpha a_2$  and  $b_2 = \alpha(a_1 + \beta a_2)$ .

The above derivation assumes a series-opposing configuration of the bias currents – that is,  $I_1$  and  $I_2$  flow in opposite directions. It is easy to verify that the series-aiding case (i.e. when  $I_1$  and  $I_2$  flow in the same direction) can be obtained by the substitution:  $\alpha \rightarrow -\alpha$  and  $\beta \rightarrow -\beta$ .

## 6.2 Quasiparticle coupling

The second coupling mechanism that we consider is the influence of a quasiparticle diffusion current from one junction on the current flow in the other junction. It can be shown that a JJ in the resistive state acts like a generator of non-equilibrium quasiparticles, and if another weak link is located within a small distance (few microns), the quasiparticles will modulate its normal current component. This is a rather rough approximation of the real phase dynamics, which does not take into account processes such as conversion between the quasiparticle and Cooper pair currents. [29]

To derive the equations describing the phase dynamics in two JJs coupled by quasiparticle currents, we follow the approach presented by Jillie et al. [22] and extend it to the noisy case. First, we include a quasiparticle current in the RSJ equation (i.e. Eq. (4.12) with  $C = 0$ ):

$$\frac{\hbar}{2eR_1} \frac{d\phi_1}{dt} = I_1 - I_{c1} \sin \phi_1 + \sqrt{\frac{2k_B T}{R_1}} \xi_1(t) + I_{q21} \quad (6.12a)$$

$$\frac{\hbar}{2eR_2} \frac{d\phi_2}{dt} = I_2 - I_{c2} \sin \phi_2 + \sqrt{\frac{2k_B T}{R_2}} \xi_2(t) + I_{q12}. \quad (6.12b)$$

Here,  $I_{qij}$  is the quasiparticle current generated by the  $i$ -th weak link and flowing through the  $j$ -th one. The total quasiparticle current generated by the second weak link is given by the right hand side of Eq. (6.12b). If we take  $\alpha_1$  to be the fraction of that current that flows through the first junction, we can write

$$I_{q21} = \alpha_1 \left( I_2 - I_{c2} \sin \phi_2 + \sqrt{\frac{2k_B T}{R_2}} \xi_2(t) + I_{q12} \right). \quad (6.13)$$

Substituting this expression into Eq. (6.12a) and following a similar procedure for  $I_{q12}$ , we obtain:

$$\begin{aligned} \frac{\hbar}{2eR_1} \frac{d\phi_1}{dt} &= I_1 - I_{c1} \sin \phi_1 + \sqrt{\frac{2k_B T}{R_1}} \xi_1(t) \\ &\quad + \alpha_1 \left( I_2 - I_{c2} \sin \phi_2 + \sqrt{\frac{2k_B T}{R_2}} \xi_2(t) \right) \\ \frac{\hbar}{2eR_2} \frac{d\phi_2}{dt} &= I_2 - I_{c2} \sin \phi_2 + \sqrt{\frac{2k_B T}{R_2}} \xi_2(t) \\ &\quad + \alpha_2 \left( I_1 - I_{c1} \sin \phi_1 + \sqrt{\frac{2k_B T}{R_1}} \xi_1(t) \right), \end{aligned}$$

where terms of second order in the coupling constants  $\alpha_i$  have been neglected. This is justified if the coupling is sufficiently weak ( $\alpha_i \ll 1$ ), which we assume is the case

here. In the noiseless case ( $\xi_1(t) = \xi_2(t) = 0$ ), this system of equations is identical to Eq. (6.5) if the following substitutions are made (values on the left hand side refer to the quasiparticle model, whereas those on the right hand side refer to the model with a resistive shunt):

$$\alpha_1 \rightarrow \alpha = \frac{R_2}{R_2 + R_3} \quad (6.14a)$$

$$\alpha_2 \rightarrow \frac{1}{\beta} = \frac{R_1}{R_1 + R_3} \quad (6.14b)$$

$$R_1 \rightarrow \frac{R_1(R_2 + R_3)}{R_1 + R_2 + R_3} \quad (6.14c)$$

$$R_2 \rightarrow \frac{R_2(R_1 + R_3)}{R_1 + R_2 + R_3}. \quad (6.14d)$$

Introducing the normalized time  $\hat{t} = t \frac{2e\bar{I}_c R_1}{\hbar}$  and measuring currents in units of  $\bar{I}_c = (I_{c1} + I_{c2})/2$  (this is the same normalization scheme as that used for the case of a resistive shunt coupling), we get

$$\begin{aligned} \frac{d\phi_1}{d\hat{t}} &= \hat{I}_1 - \hat{I}_{c1} \sin \phi_1 + \sqrt{D_0} \xi_1(t) \\ &\quad + \alpha_1 \left( \hat{I}_2 - \hat{I}_{c2} \sin \phi_2 + \sqrt{D_0 \frac{R_1}{R_2}} \xi_2(t) \right) \\ \frac{R_1}{R_2} \frac{d\phi_2}{d\hat{t}} &= \hat{I}_2 - \hat{I}_{c2} \sin \phi_2 + \sqrt{D_0 \frac{R_1}{R_2}} \xi_2(t) \\ &\quad + \alpha_2 \left( \hat{I}_1 - \hat{I}_{c1} \sin \phi_1 + \sqrt{D_0} \xi_1(t) \right), \end{aligned}$$

with the dimensionless noise strength  $D_0 = \frac{4ek_B T}{\bar{I}_c \hbar}$ . As usual, we shall drop the hat signs in subsequent equations, in which it will be implicitly assumed that currents and time are normalized. Using the noise addition rule Eq. (2.11), these equations can be rewritten as:

$$\frac{d\phi_1}{dt} = I_1 - I_{c1} \sin \phi_1 + \alpha_1 (I_2 - I_{c2} \sin \phi_2) + \sqrt{D_0 \left( 1 + \alpha_1^2 \frac{R_1}{R_2} \right)} \xi'(t) \quad (6.15a)$$

$$\frac{R_1}{R_2} \frac{d\phi_2}{dt} = I_2 - I_{c2} \sin \phi_2 + \alpha_2 (I_1 - I_{c1} \sin \phi_1) + \sqrt{D_0 \left( \frac{R_1}{R_2} + \alpha_2^2 \right)} \xi''(t). \quad (6.15b)$$

We might observe that the noise intensities in Eq. (6.15) do not match those in Eq. (6.10). For example, if we use Eq. (6.14a) for the  $\xi'(t)$  intensity, we obtain  $\sqrt{D_0(\beta + \alpha)/\beta}$ ,

whereas in the model with a resistive shunt, the intensity used to be simply  $\sqrt{D_0}$ . Such discrepancies are however to be expected, as previously we considered also the noise from the shunt resistor, which is absent from the quasiparticle interaction model.

In the remaining part of this chapter, we will be using the notation for the model with a resistive shunt, i.e. Eq. (6.11).

### 6.3 Identical junctions

We first consider the special case of two identical junctions, for which  $R_1 = R_2$  and  $I_{c1} = I_{c2}$  in Eq. (6.11). This implies that in our system of units  $I_{c1} = I_{c2} = 1$ ,  $\alpha\beta = 1$ , and  $b_2 = a_2 + \alpha a_1$ . The system (6.11) becomes

$$\frac{d\phi_1}{dt} = I_1 - I_{c1} \sin \phi_1 + \alpha (I_2 - I_{c2} \sin \phi_2) + \sqrt{D_0} \xi'(t) + (a_1 + \alpha a_2) \cos(\omega t) \quad (6.16a)$$

$$\frac{d\phi_2}{dt} = I_2 - I_{c2} \sin \phi_2 + \alpha (I_1 - I_{c1} \sin \phi_1) + \sqrt{D_0} \xi''(t) + (a_2 + \alpha a_1) \cos(\omega t), \quad (6.16b)$$

which is symmetric with regard to junction interchange.

The parameter space of the system  $\{\alpha, a_1, a_2, I_1, I_2, \omega\}$  is 6-dimensional and thus too large to extensively scan numerically. To analyze this system, we followed a scheme similar to that used in the case of a single JJ in Chapter 5. First, a number of low resolution scans over the parameters  $\{\alpha, a_1, a_2, \omega\}$  at fixed values of  $I_1$  and  $I_2$  was performed, and then the interesting areas of the parameter space were analyzed in more detail and at a higher resolution. These initial scans were done for the noiseless case ( $D_0 = 0$ ), for initial values of the phases  $\phi_1$  and  $\phi_2$  randomly chosen from the range  $[0; 2\pi]$ . They were then supplemented by scans at non-zero temperatures.

#### 6.3.1 Dynamics overview

We begin the analysis of the dynamics of the system by some general remarks about its behavior under different driving conditions. We have found that the modulus of the average velocity for both particles takes its highest values for  $\omega \in (0, 1]$  and is gradually diminished for higher frequencies. At large AC driving frequencies ( $\omega > 5$ ) there is no net transport regardless of the values of other parameters.

#### 6.3.2 AC driving applied to a single junction

If only the first particle is biased and driven by an oscillating force ( $a_1 > 0, I_1 > 0, a_2 = I_2 = 0$ ), strips of non-zero average velocity are clearly visible in the parameter space. For low values of  $\alpha$ , there is no net transport for the second particle, but for higher

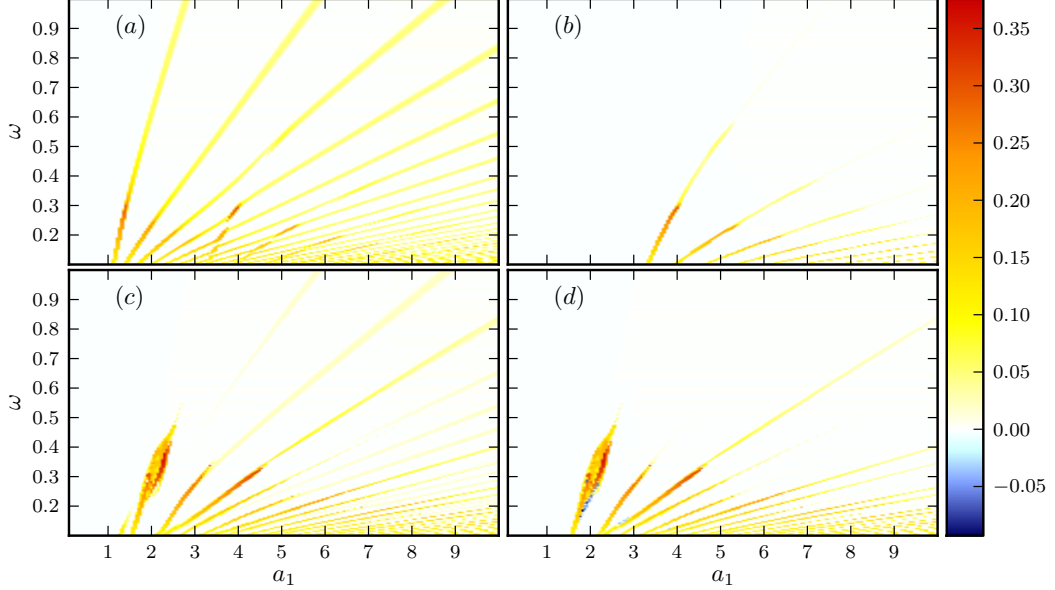


Figure 6.2: Transport properties of a system of two identical JJs with a DC bias and AC driving on the first junction.  $I_1 = 0.05$ . Panels (a), (b):  $\alpha = 0.359$ ;  $\langle v_1 \rangle, \langle v_2 \rangle$ , respectively. Panels (c), (d):  $\alpha = 0.763$ ;  $\langle v_1 \rangle, \langle v_2 \rangle$ , respectively.

values strips of non-zero average velocity start to appear at progressively lower values of  $a_1$ . These strips are also visible in the plots of the average velocity of the first particle, which means that they represent areas of the parameter space where both particles move in synchrony (see Figure 6.2(a),(b)). For  $\alpha \in [0.66; 0.9]$  and  $a_1 \approx 2.0 \pm 0.5$  the structures visible in the plots become more complex and areas of negative mobility of the second particle can be identified (see Figure 6.2(c),(d)).

A more careful investigation of the parameter area where negative mobility appears, reveals a rich structure (see Figure 6.3(a)), which is gradually washed away by increasing temperature (see Figure 6.3(b)-(d)).

Having identified a parameter area exhibiting negative mobility, it is instructive to look at the system dynamics when it is subject to a very low and zero DC bias  $I_1$ . As expected from the symmetry of the system (6.16), in the zero bias case there is no net transport. However, the inspection of the average modulus of velocity (Figure 6.4(a)) reveals areas of the parameter space where attractors for both positive and negative velocity exist for both particles. At very low values of  $I_1$  (up to about 0.01), the velocities of both particles are nearly identical. Figure 6.4 suggests that for low  $I_1$  the areas of negative and positive mobility have a direct relation to the attractors at zero bias. For larger values of  $I_1$ , where the velocities  $\langle v_1 \rangle$  and  $\langle v_2 \rangle$  start to diverge, this is less obvious, though some structures that were present at zero bias are still recognizable (see Figure 6.5). For

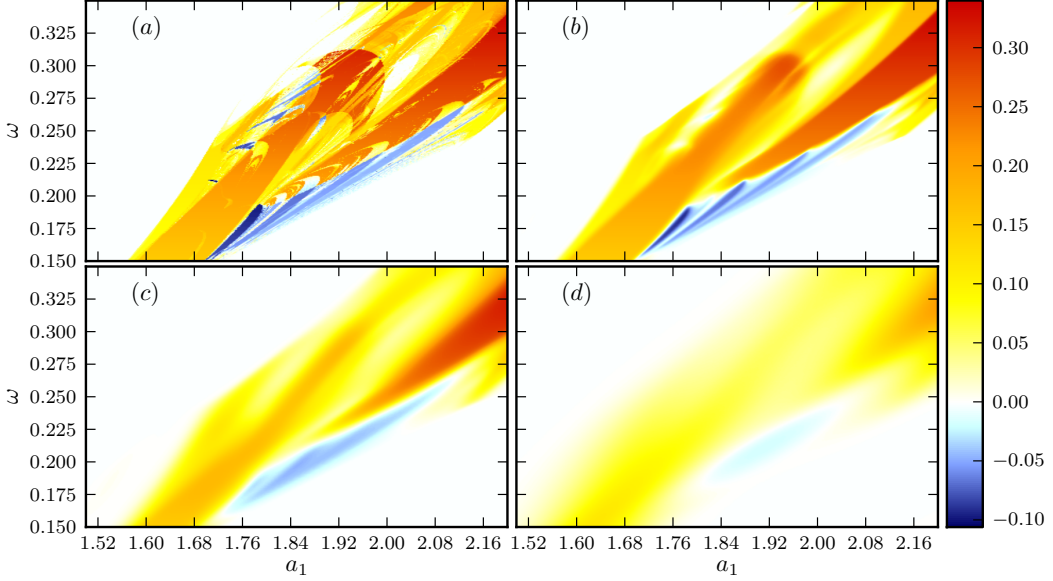


Figure 6.3: Anomalous transport properties of the second particle at various temperatures.  $\alpha = 0.77$ ,  $a_2 = I_2 = 0$ ,  $I_1 = 0.05$ . Panels (a)-(d):  $D_0 = 0, 5 \cdot 10^{-5}, 2.5 \cdot 10^{-4}, 2.5 \cdot 10^{-3}$ , respectively.

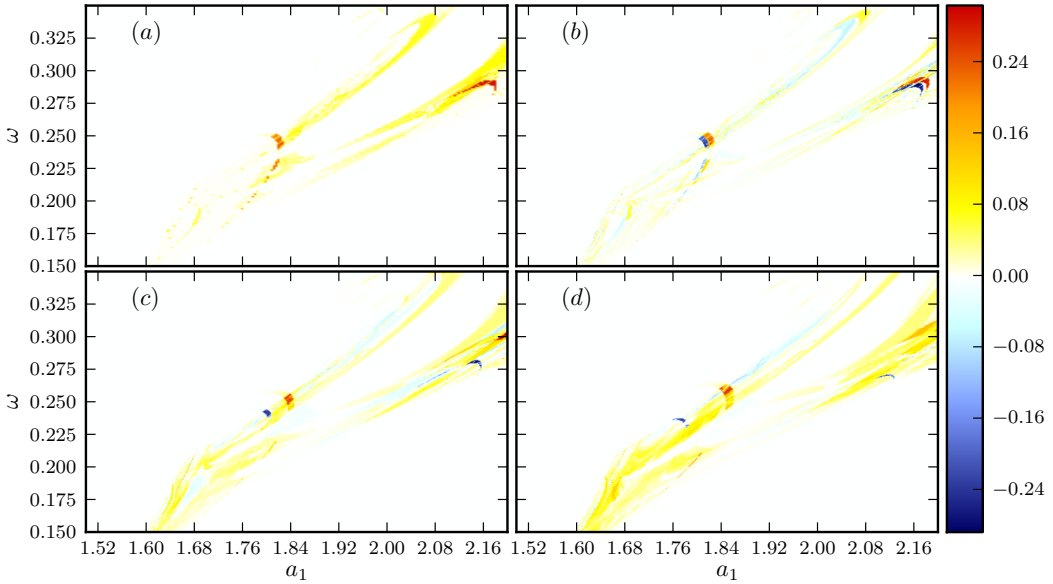


Figure 6.4: Average velocity of the first particle for very low DC bias  $I_1$ .  $\alpha = 0.77$ ,  $D_0 = 0$ ,  $a_2 = I_2 = 0$ . Panel (a):  $I_1 = 0$ , average modulus of velocity is shown. Panels (b)-(d):  $I_1 = 0.001, 0.005$  and  $0.01$ , respectively. Average velocity is shown.

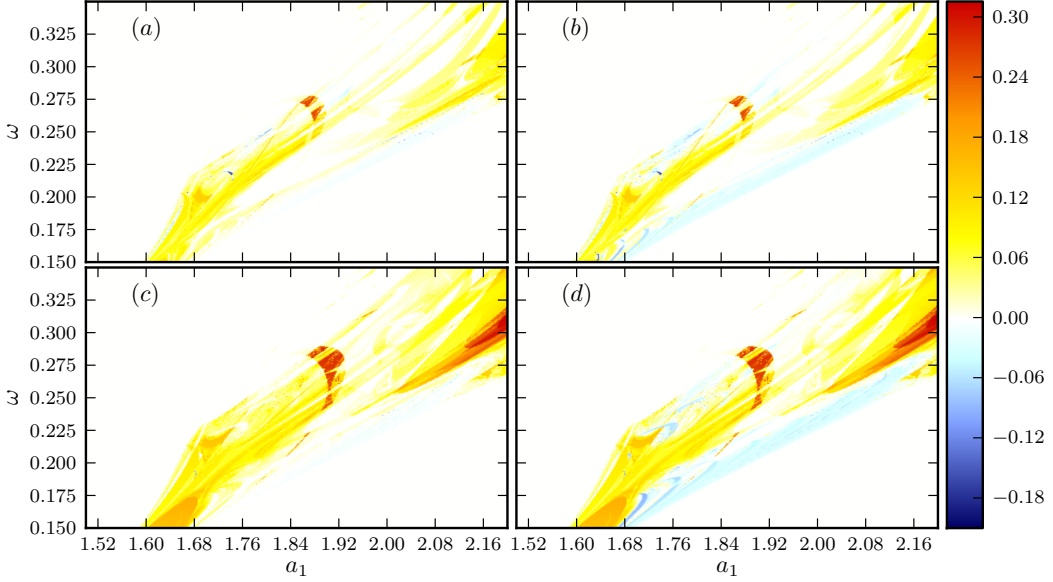


Figure 6.5: Average velocities for low DC bias  $I_1$ .  $\alpha = 0.77$ ,  $D_0 = 0$ ,  $a_2 = I_2 = 0$ . Panels (a)-(b):  $I_1 = 0.02$ ;  $\langle v_1 \rangle$  and  $\langle v_2 \rangle$ , respectively. Panels (c)-(d): same, but for  $I_1 = 0.03$ .

the area of the parameter space presented in Figure 6.5, negative mobility of the first particle exists up to about  $I_1 = 0.05$ . At larger DC bias values, only the second particle exhibits negative mobility. In the series-aiding configuration, the roles of the negative and positive mobility areas for the second particle are approximately reversed. No such changes take place for the first particle. That the reversal is only approximate is clear if we note that in Eq. (6.16b) all but one terms have the prefactor  $\alpha$ , which changes its sign when the system is switched to the series-aiding case.

Figure 6.3 already suggests that the system exhibits a very rich dynamics and that different types of anomalous response might be possible. This is confirmed by selecting specific points in the parameter space and looking at their load-response curves at different temperatures. We were able to find regions of the parameter space where only the second particle exhibited ANM (see Figure 6.6), where both particles exhibited ANM and where the effect was noise-induced (see Figure 6.7), as well as areas where the NNM and NDM effects were exhibited by one or two particles (see Figure 6.8 and Figure 6.9). We did not find any areas of the parameter space where only the *first* particle would exhibit ANM in the series-opposing case of the bias configuration. In the series-aiding case on the other hand, there are areas where only the first or only the second particle moves against a DC bias  $I_1$ , but there are no areas where both particles exhibit negative mobility simultaneously.

The anomalous transport effects discussed above are all caused by the coupling between

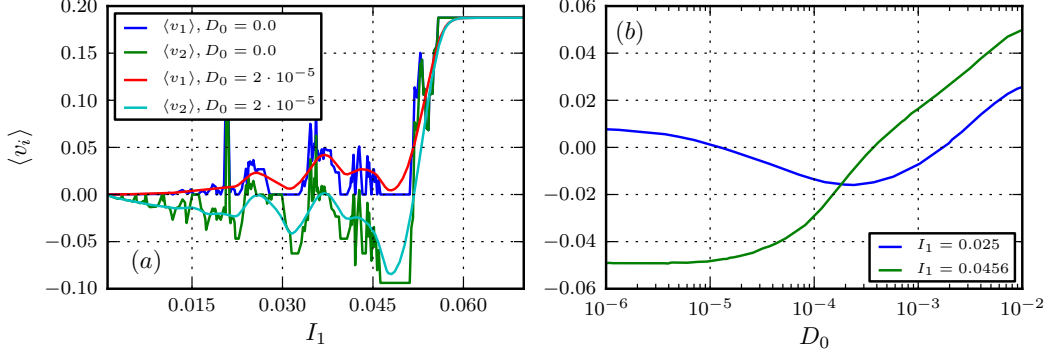


Figure 6.6: Deterministic ANM of the second particle gradually destroyed by noise. Panel (b) depicts the dependence of  $\langle v_2 \rangle$  on the temperature for two values of  $I_1$ . Parameters are:  $\omega = 0.1876$ ,  $a_1 = 1.7754$ ,  $a_2 = I_2 = 0.0$ ,  $\alpha = 0.77$ .

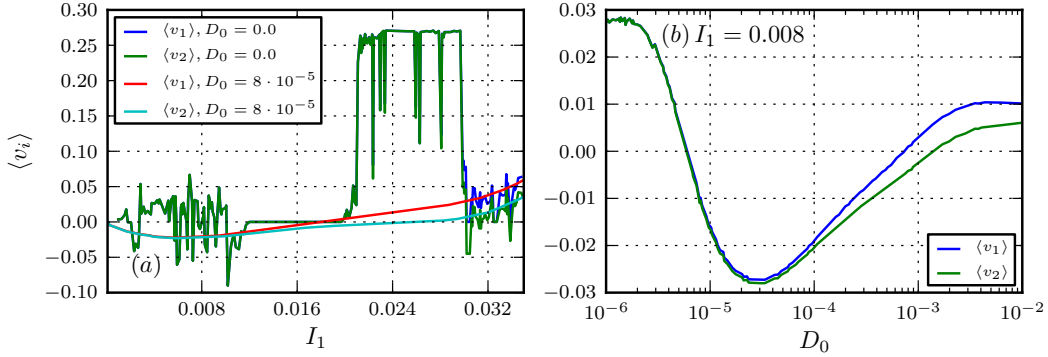


Figure 6.7: Noise-induced ANM of both particles. Parameters are:  $\omega = 0.2708$ ,  $a_1 = 1.8912$ ,  $a_2 = I_2 = 0.0$ ,  $\alpha = 0.77$ .

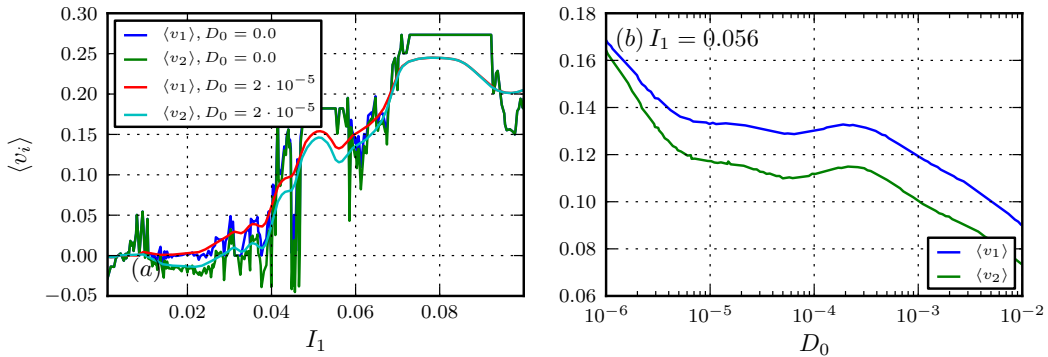


Figure 6.8: NNM and NDM of both particles. Parameters are:  $\omega = 0.2733$ ,  $a_1 = 2.1614$ ,  $a_2 = I_2 = 0.0$ ,  $\alpha = 0.77$ .

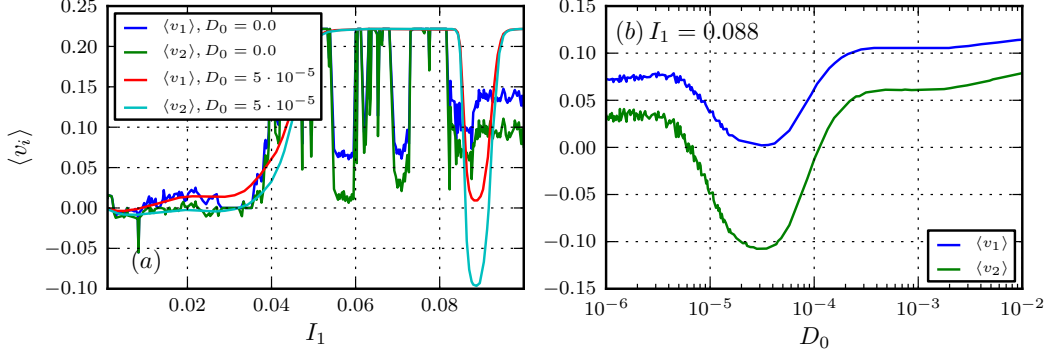


Figure 6.9: Strong NNM and weak ANM of the second particle, as well as strong NDM of both particles. Parameters:  $\omega = 0.2217$ ,  $a_1 = 1.9088$ ,  $a_2 = I_2 = 0.0$ ,  $\alpha = 0.77$ .

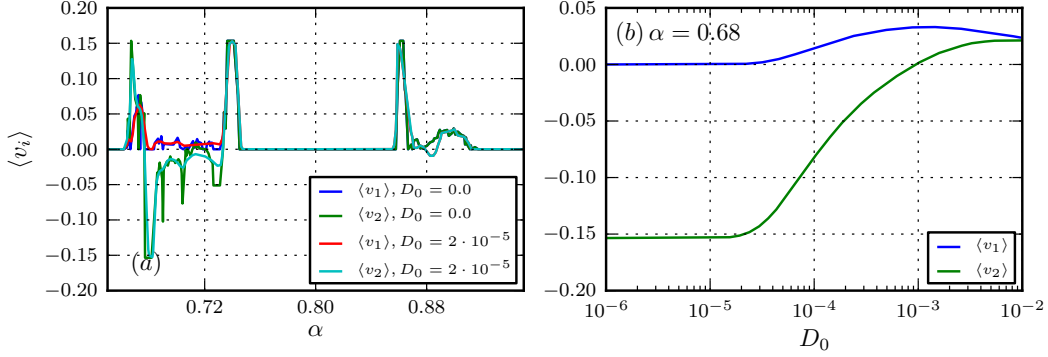


Figure 6.10: Influence of  $\alpha$  on the negative mobility of the second particle at  $I_1 = 0.01$ . Other parameters are  $\omega = 0.1535$ ,  $a_1 = 2.4860$ ,  $a_2 = I_2 = 0.0$ .

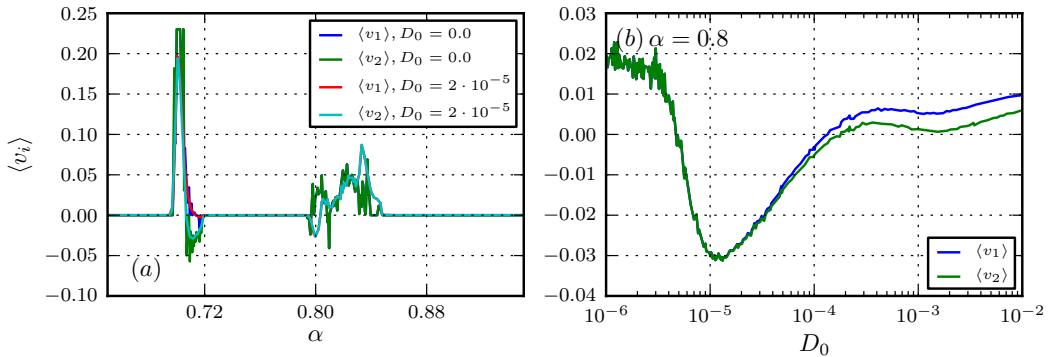


Figure 6.11: Influence of  $\alpha$  on the negative mobility of both particles at  $I_1 = 0.01$ . Other parameters are  $\omega = 0.2303$ ,  $a_1 = 2.0$ ,  $a_2 = I_2 = 0.0$ .

the particles. As discussed in Chapter 5, no anomalous transport is possible in a system described by a first order non-autonomous stochastic differential equation under reasonable assumptions about the drift and diffusion coefficients. Figure 6.10 and Figure 6.11 show how the average velocity of both particles depends on the coupling constant  $\alpha$ , in cases when only one of the particles exhibits negative mobility, and when both particles do so. We can see that there are always finite windows of  $\alpha$  for which this effect can be observed.

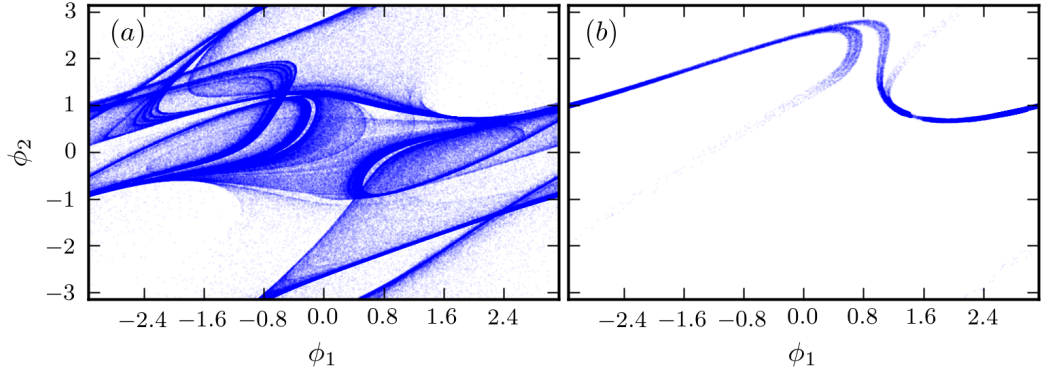


Figure 6.12: Panel (a): phase portrait of the system (6.16) at  $I_1 = 0.0456$ ,  $I_2 = 0.0$ ,  $\omega = 0.1876$ ,  $a_1 = 1.7754$ ,  $a_2 = 0$ ,  $\alpha = 0.77$ ,  $D_0 = 0$ . The parameters correspond to Figure 6.6. Panel (b): same parameters, Poincaré section at the beginning of each driving period. 250000 driving periods are plotted.

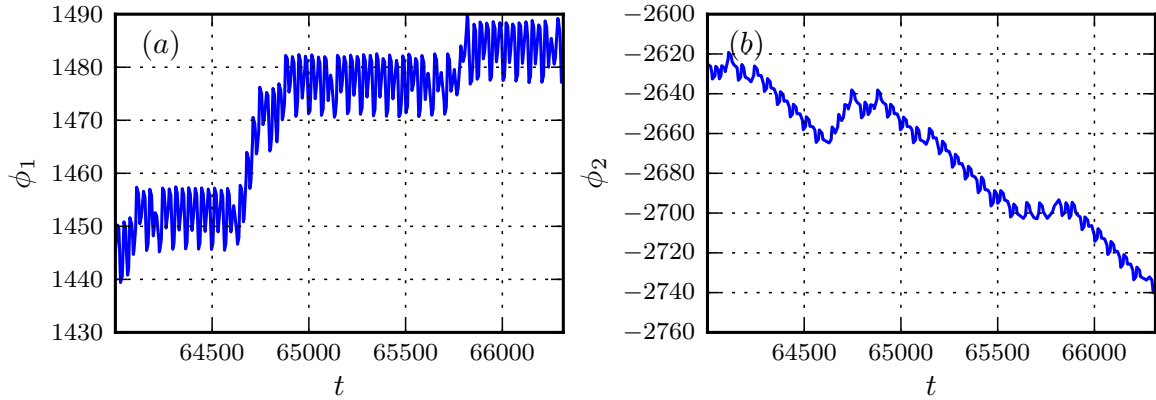


Figure 6.13: Sample trajectories for the noiseless system (6.16). Parameters are as in Figure 6.12. Panel (a) depicts the trajectory of the first particle, while panel (b) depicts that of the second particle.

More details about the dynamics of the system are revealed by its phase portraits, as well as by the individual trajectories. The irregularity of the profiles in Figure 6.6–Figure 6.11

at  $D_0$  suggests that the phase dynamics of the system is chaotic for the depicted sets of parameters. This conjecture is confirmed in Figure 6.12, where the phase portrait as well as a Poincaré section are depicted. The attractor visible on the Poincaré section appears to be deceptively simple, unlike typical strange attractors of chaotic systems. However, it is enough to confirm that the motion of the system is not periodic – if it were, we would expect to see a single point or a few fixed points on the Poincaré section. The phase portrait in Figure 6.12(a) shows that the system moves around a large part of the phase space, and the trajectories in Figure 6.13 confirm that the motion is indeed chaotic.

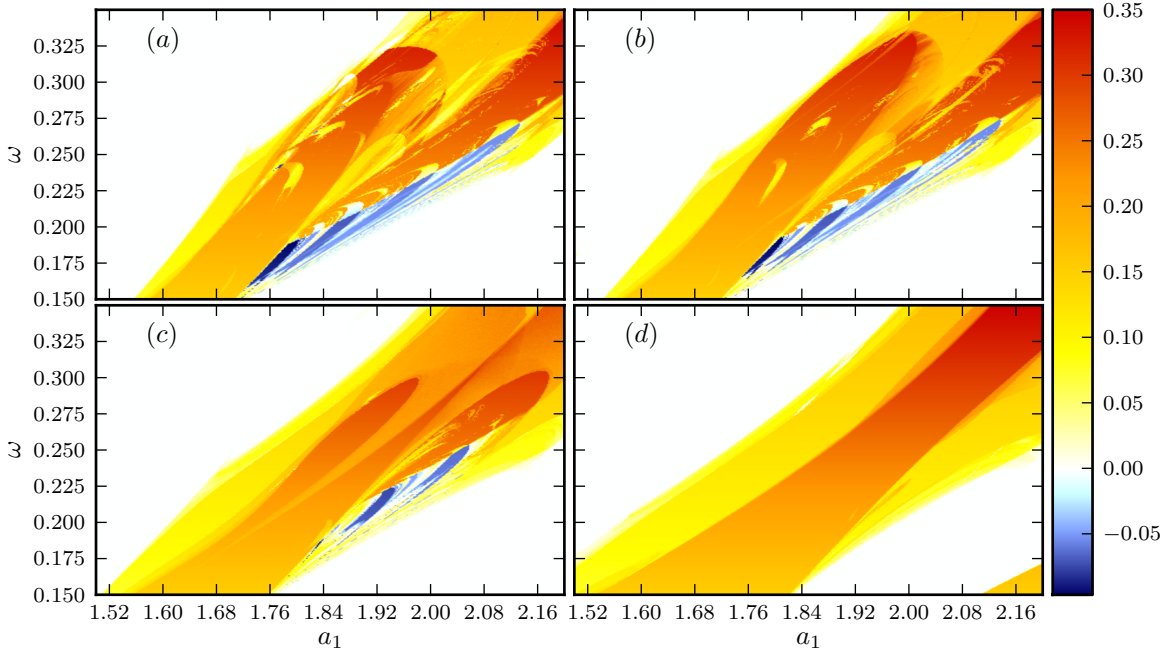


Figure 6.14: Impact of DC bias on the second particle.  $\alpha = 0.77$ ,  $I_1 = 0.05$ ,  $D_0 = 0$ . Panels (a)-(d):  $I_2 = 0.01, 0.02, 0.05, 0.1$ , respectively.

Adding a constant bias to the second particle has a destructive impact on the negative mobility (see Figure 6.14) – the higher the value of  $I_2$ , the smaller the parameter area where negative mobility can be observed. The small areas of negative mobility located in the parameter ranges  $(a_1, \omega) \in [1.7; 1.9] \times [0.22; 0.30]$  are extinguished first – they are already gone at  $I_2 = 0.02$  (see Figure 6.14(b)). We find 0.1 to be the limiting value of  $I_2$  at which areas of negative mobility cease to exist everywhere in the analyzed area when  $I_1 = 0.05$ .

From Figure 6.14 it is evident that increasing  $I_2$  has a general smoothing effect on the transport properties of the second particle – at higher values of  $I_2$ , the fine details visible in Figure 6.3(d) gradually disappear. Increasing  $I_2$  also causes all features to

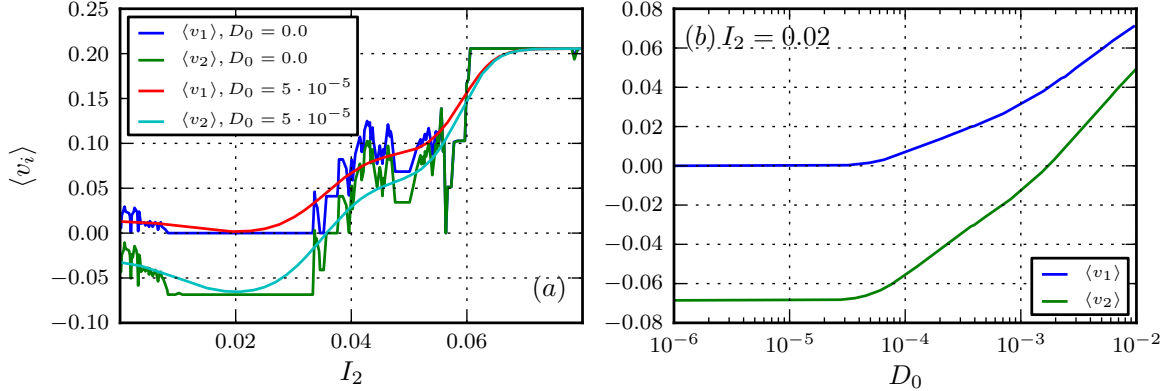


Figure 6.15: DC bias on the second particle increasing strength of a negative mobility effect exhibited by that particle. Parameters are:  $\alpha = 0.77$ ,  $a_1 = 1.8807$ ,  $\omega = 0.2056$ ,  $I_1 = 0.05$ .

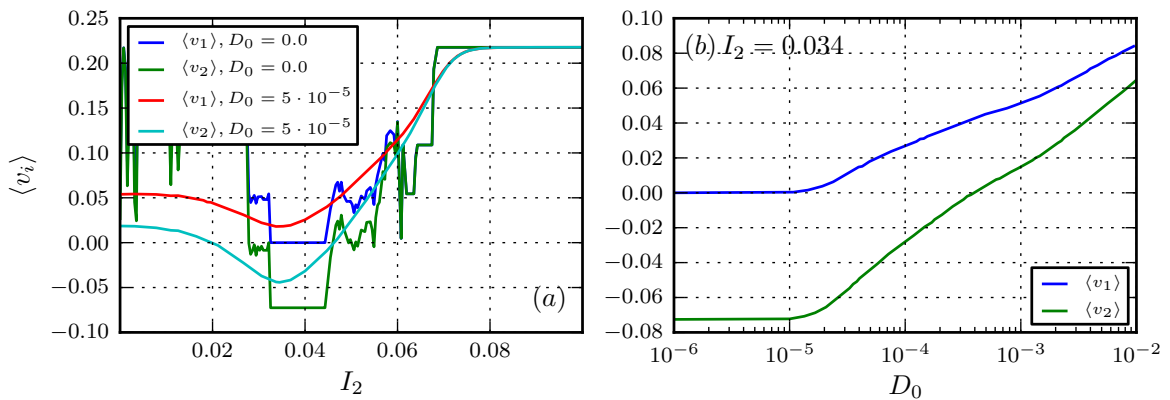


Figure 6.16: DC bias on the second particle creating a negative mobility effect of that particle. Parameters are:  $\alpha = 0.77$ ,  $a_1 = 1.9158$ ,  $\omega = 0.2177$ ,  $I_1 = 0.05$ .

move slightly towards higher values of  $a_1$  and  $\omega$ . It is therefore possible to find areas of the parameter space where  $I_2$  induces a negative mobility effect (Figure 6.16), as well as areas where it increases the strength of an existing negative mobility effect (Figure 6.15).

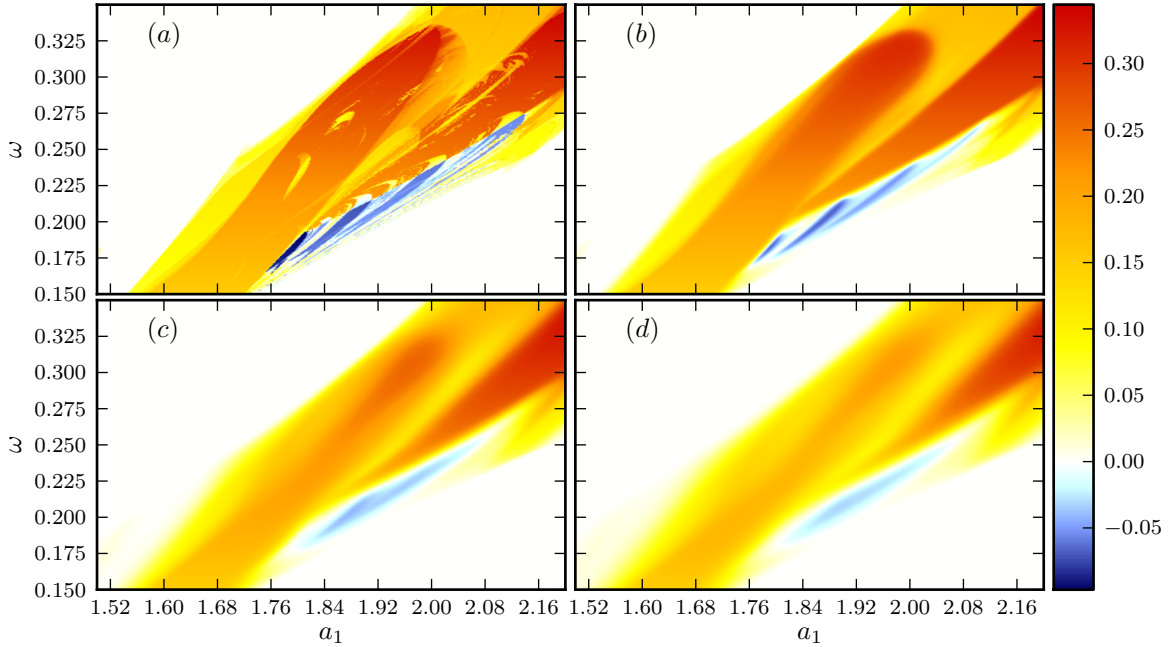


Figure 6.17: Impact of DC bias ( $I_2 = 0.02$ ) on the second junction at non-zero temperature. Panels (a)-(d):  $D_0 = 0, 5 \cdot 10^{-5}, 5 \cdot 10^{-4}, 2.5 \cdot 10^{-4}$ , respectively.

When noise is added to the system, we again see a smoothing effect (see Figure 6.17), with larger temperatures completely destroying the anomalous transport effects. The explanation of the smoothing is the same as in the case of a single JJ – noise causes random transitions between coexisting basins of attraction.

### 6.3.3 AC driving applied to both junctions

We begin with some general remarks about the dynamics gained from comprehensive scans of the parameter space. The striped structure of transport regions of  $\langle v_1 \rangle$  is generally preserved in the presence of  $a_2 \neq 0$ . Increasing  $a_2$  causes the strips to move towards lower values of  $a_1$  on the  $(a_1, \omega)$  plot, as seen in Figure 6.18.

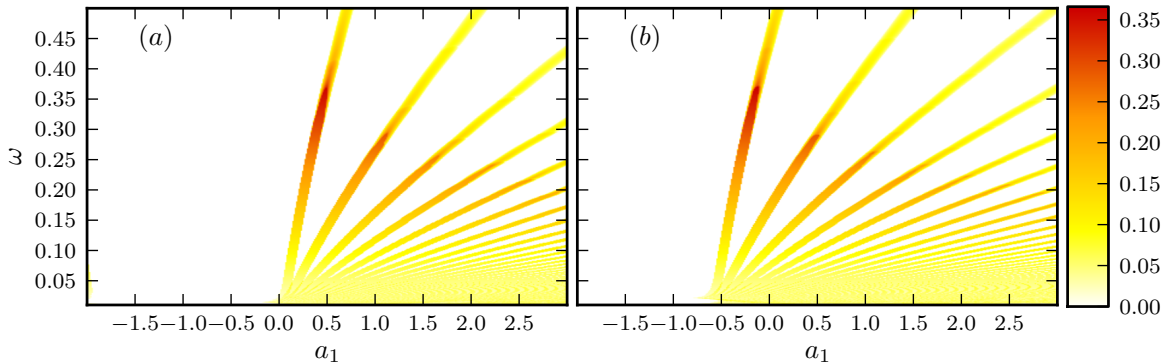


Figure 6.18: Transport properties of the first particle for large values of  $a_2$ .  $\alpha = 0.2$ .  
Panel (a):  $a_2 = 5.0$ , panel (b):  $a_2 = 8.0$ .

For values of  $a_2$  comparable to that of  $a_1$ , the influence of the AC driving on the second particle could be described as causing ripples on the strips in the areas of  $\langle v_1 \rangle$  (see Figure 6.19).

The behavior of  $\langle v_2 \rangle$  is slightly more complex, with areas of non-zero transport appearing in places of intersection of two sets of strips, one bent towards the lower values of  $a_1$ , and the other one towards larger values of  $a_1$  (see Figure 6.20).

We were able to detect several areas of negative mobility of the second particle (see Figure 6.20 and Figure 6.21 for a close-up view). There appear to be two distinguishable kinds of areas of negative mobility, which also appear for different combinations of  $a_1$ ,  $a_2$  and  $\omega$  (see Figure 6.20). The first type is formed by multiple thin bundles of negative mobility (Figure 6.21(a)), while the second type covers a larger area of the parameter space in a more uniform way (Figure 6.21(b)).

As usual, adding noise to the system results in a smoothing of the plot (see Figure 6.22).

We also investigated the impact of AC driving on the second particle for the ranges of parameters analyzed in the previous subsection and depicted in Figure 6.3. The results can be seen in Figure 6.23. While the general effect of increasing  $a_2$  is a decrease in the area of parameters resulting in negative transport, there are some values of  $a_2$  that result in an actual increase of the rate of the negative transport (compare minimal value of  $\langle v_2 \rangle$  in Figure 6.23(a) with Figure 6.23(c)).

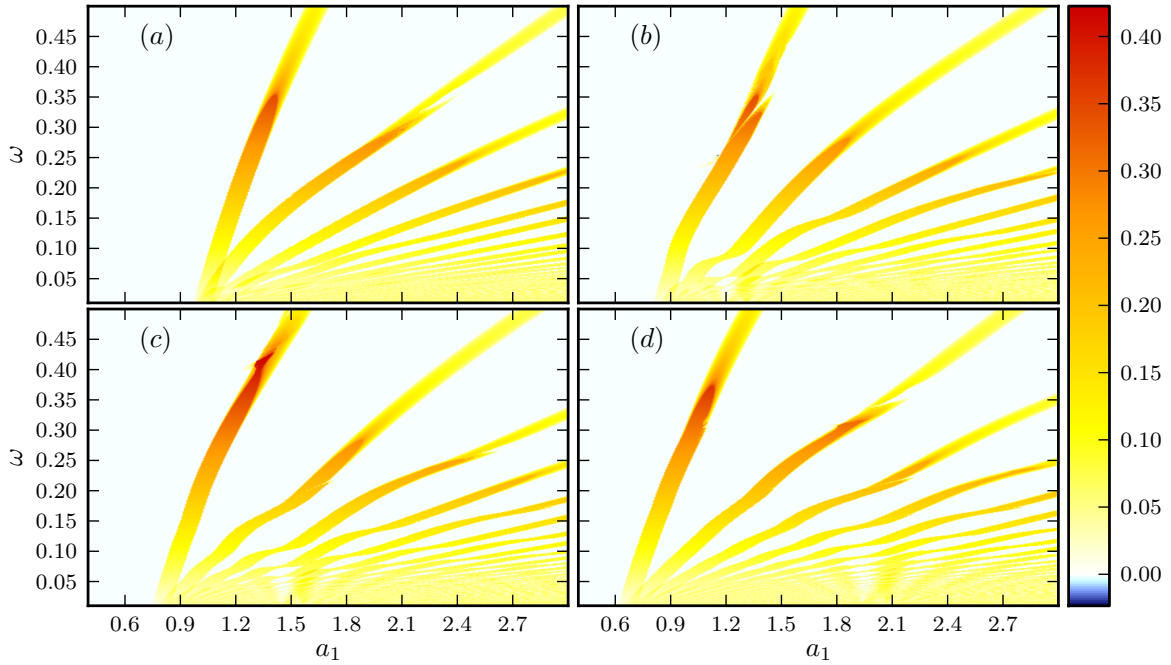


Figure 6.19: Transport properties of the first particle for values of  $a_2$  comparable to those of  $a_1$ .  $\alpha = 0.2$ . Panels (a)-(d):  $a_2 = 1.0, 1.25, 1.5, 2.0$ , respectively.

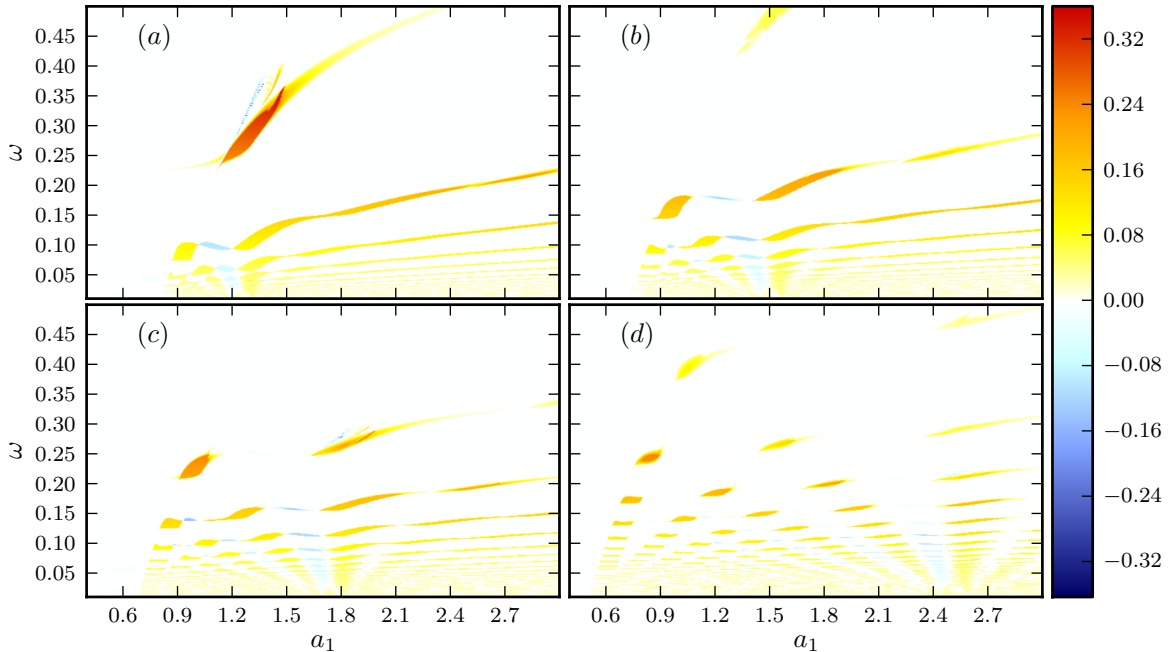


Figure 6.20: Transport properties of the second particle for values of  $a_2$  comparable to those of  $a_1$ .  $\alpha = 0.2$ . Panels (a)-(d):  $a_2 = 1.25, 1.5, 1.75, 2.5$ , respectively.

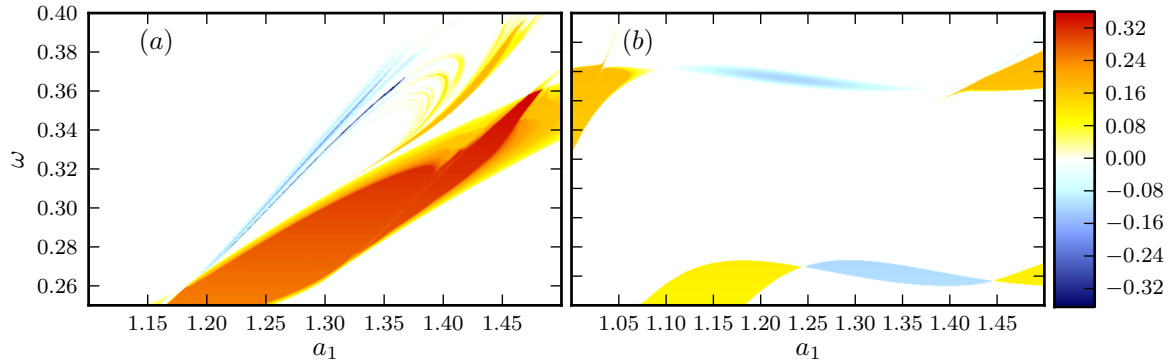


Figure 6.21: Close-up view of the areas of the parameter space exhibiting negative transport.  $\alpha = 0.2, D_0 = 0$ . Panel (a):  $a_2 = 1.25$ , panel (b):  $a_2 = 1.5$ .

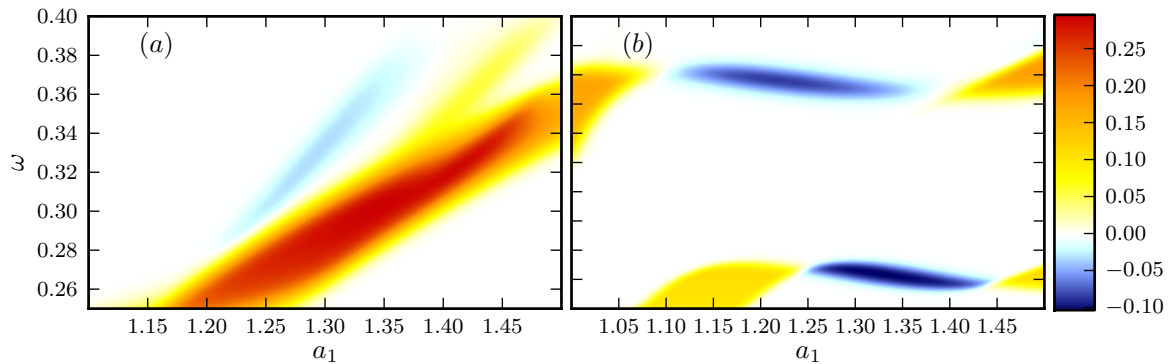


Figure 6.22: Close-up view of the areas of the parameter space exhibiting negative transport.  $\alpha = 0.2, D_0 = 0.0001$ . Panel (a):  $a_2 = 1.25$ , panel (b):  $a_2 = 1.5$ .

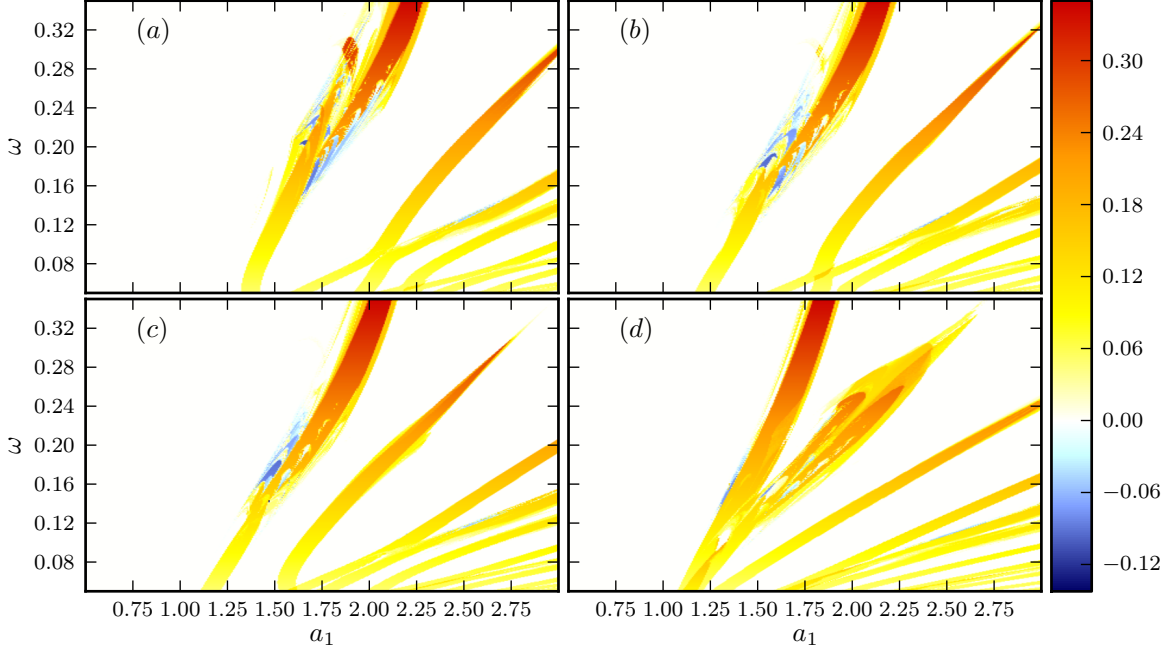


Figure 6.23: Transport properties of the second particle for low  $a_2$ .  $\alpha = 0.77, I_1 = 0.05$ . Panels (a)-(d):  $a_2 = 0.05, 0.15, 0.25, 0.5$ , respectively.

## 6.4 Two different junctions

The parameter space when two different junctions are considered is 9-dimensional  $\{I_1, I_2, I_{c1}, D_0, \alpha, \beta, \omega, b_1, b_2\}$  and too large to analyze numerically in a systematic fashion. We therefore decided to focus our attention on the effects of the coupling constants  $\alpha$  and  $\beta$ , and on the impact of slight variations of the junction parameters on the negative mobility effects described in the previous sections.

We performed extensive numerical scans over  $\alpha$  and  $\beta$ , at equal AC driving intensities  $b_1 = b_2 = b$  and with  $I_1 = 0.05, I_2 = 0.0, D_0 = 0$  and  $I_{c1} = I_{c2} = 1$ . These allowed us to determine that on  $(b, \omega)$  cuts the areas of non-zero mobility of both particles form striped structures, similar to those seen for the system of two identical junctions. We were able to find areas of negative mobility of the first particle for  $\alpha \geq 0.2$  and approximately  $\alpha\beta \leq 1$ . If  $\alpha$  is kept at a constant value while  $\beta$  is steadily increased, distortions moving along the strips can be seen. While  $\beta$  is being increased, areas of negative mobility first appear in a distorted part of the strips. They then become smaller and smaller as  $\beta$  grows further. At even larger  $\beta$ , some areas of negative mobility of the first particle can then be seen at low values of  $\omega$  (smaller than approximately 0.1).

The dynamics of the second particle is similar, but the order of appearance of negative mobility areas is reversed. As  $\beta$  is increased, they first appear at low values of  $\omega$ . At

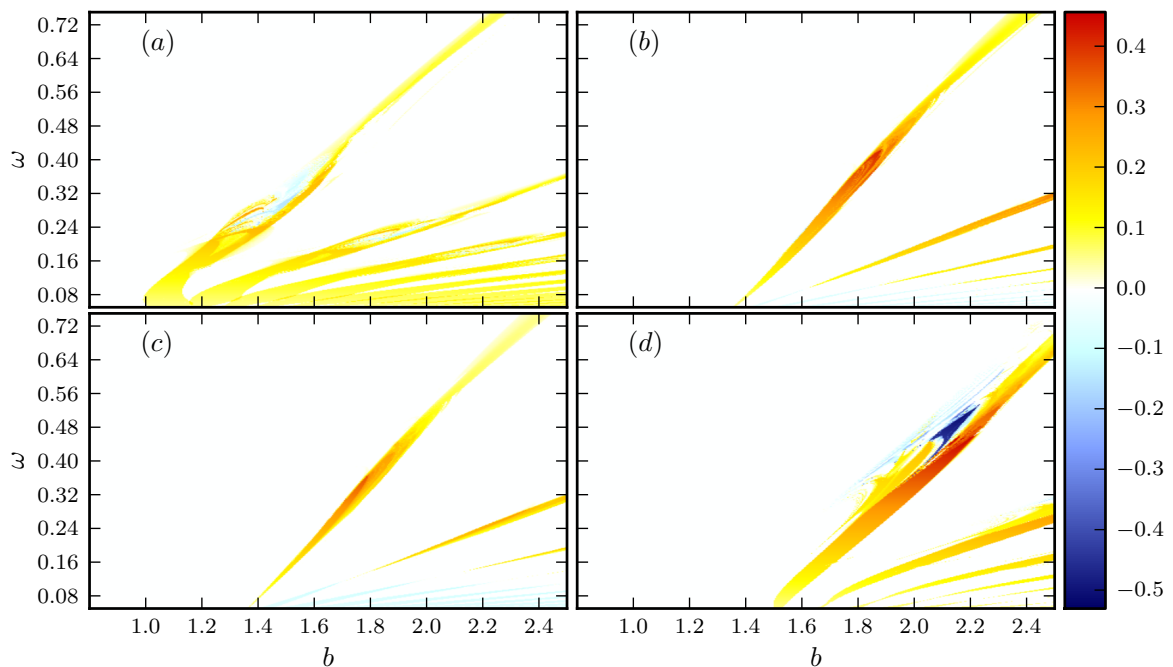


Figure 6.24: Average velocities for different values of  $\beta$ .  $I_{c1} = I_{c2} = 1$ ,  $I_2 = 0$ ,  $\alpha = 0.45$ ,  $I_1 = 0.05$ ,  $D_0 = 0$ . Panel (a):  $\langle v_1 \rangle$ ,  $\beta = 1.17$ , panels (b)-(c):  $\beta = 2$ ,  $\langle v_1 \rangle, \langle v_2 \rangle$ , respectively; panel (d):  $\beta = 3$ ,  $\langle v_2 \rangle$ .

higher values of  $\beta$ , negative mobility is visible near some of the distortions in the strips. At  $\alpha\beta \gg 1$ , no negative mobility is observed. Representative examples of the behavior described above are presented in Figure 6.24.

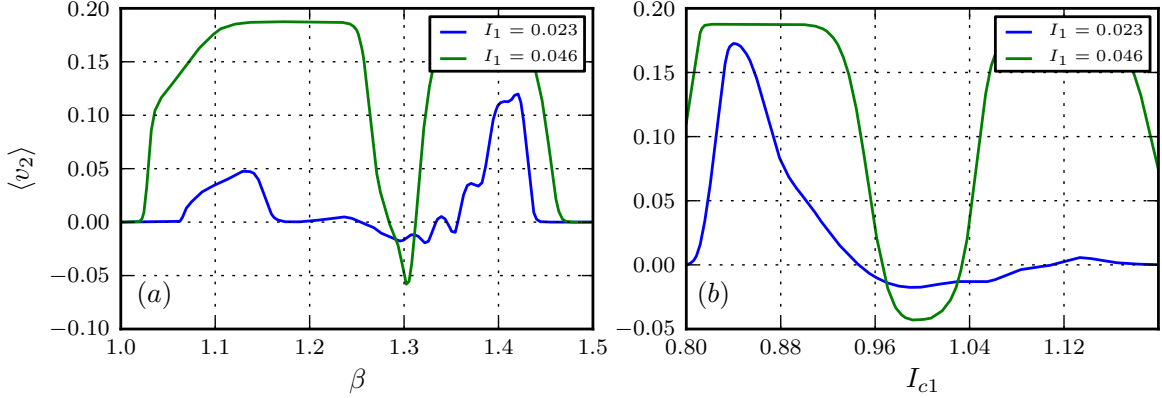


Figure 6.25: Stability of the negative mobility effects upon variation of the parameters  $\beta$  and  $I_{c1}$ .  $D_0 = 5 \cdot 10^{-5}$ . Remaining parameters are as in Figure 6.6.

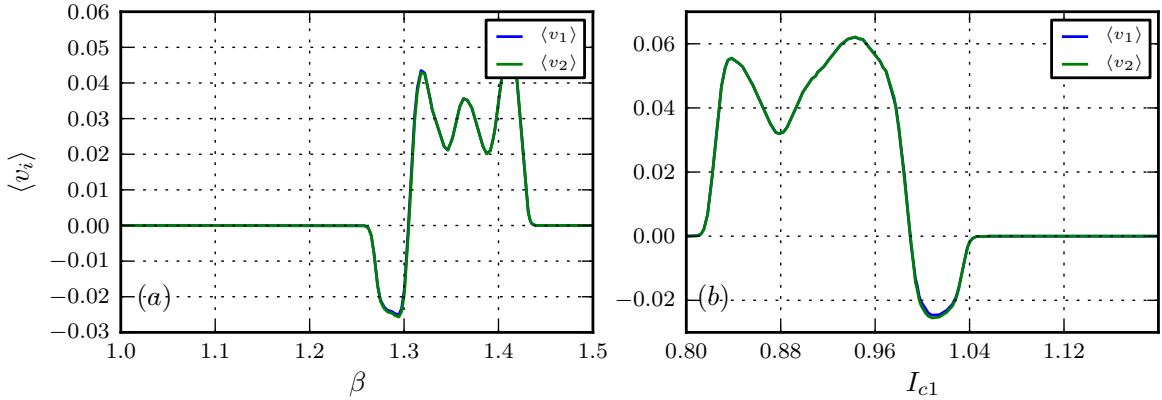


Figure 6.26: Stability of the negative mobility effects upon variation of the parameters  $\beta$  and  $I_{c1}$ .  $D_0 = 8 \cdot 10^{-5}$ . Remaining parameters are as in Figure 6.7.

Having determined the general behavior when the  $\beta$  parameter is changed, we decided to investigate the stability of the negative mobility effects uncovered for the system of two identical JJs upon variations of the parameters  $\beta$  and  $I_{c1}$ , which correspond to changes in the junction resistances and critical currents, respectively. The dependence on the average velocity on changes in these two parameters is presented in Figure 6.25 and in Figure 6.26, which correspond to the parameter sets from Figure 6.6 and in Figure 6.7. As could be expected, we find that the negative mobility effects appear over a rather limited ranges of  $\beta$ , and  $I_{c1}$ , but in both cases that were investigated the changes in the

average velocity are never abrupt and thus the anomalous effects could be said to be stable provided the variations are small. It should also be noted, that the effects are most pronounced for the case of *identical* junctions, with any differences between them diminishing the negative conductance.

## 6.5 Interpretation in the RSJ model

In this subsection we outline the procedure of scaling the dimensionless variables used in the simulations back to their physical values. This is important when one wants to design an experiment to test the results obtained through numerical calculations. Using the definitions from the beginning of this chapter, it is easy to see that the following relations hold:

$$T = \frac{E_J}{2k_B} D_0, \quad (6.17)$$

$$\Omega = \omega \frac{2eV_0}{\hbar}, \quad (6.18)$$

$$R_3 = R \frac{1 - \alpha}{\alpha}, \quad (6.19)$$

$$R = \frac{V_0}{I_c} (\alpha + 1), \quad (6.20)$$

where  $\Omega$  is the physical frequency of the external AC driving, and  $R = R_1 = R_2$  is the resistance of the two JJs. Furthermore, we have

$$I_{DC} = I_c I_1, \quad I_{AC} = I_c a_1, \quad V_i = V_0 \langle v_i \rangle \quad (6.21)$$

We shall now use the above relations to calculate physical quantities corresponding to the parameter set from Figure 6.6, that is  $\omega = 0.1876$ ,  $a_1 = 1.7754$ ,  $a_2 = I_2 = 0.0$ ,  $\alpha = 0.77$ ,  $D_0 = 5 \cdot 10^{-5}$ .

1. Set the desired temperature, e.g. 10 K.
2. Use Eq. (6.17) to calculate  $E_J$  and the critical current  $I_c \approx 16.780$  mA.
3. Calculate the driving amplitude and the bias amplitude using Eq. (6.21):  $I_{AC} \approx 27.972$  mA,  $I_{DC} \approx 0.771$  mA.
4. Set the frequency of the incident microwave radiation, e.g.  $\Omega = 100$  GHz.
5. Calculate the voltage  $V_0$  using Eq. (6.18) and use it calculate the physical voltage with Eq. (6.21):  $V \approx -0.0158$  mV.
6. Calculate the resistance of the junction using Eq. (6.20):  $R = 18.50$  m $\Omega$ .
7. Calculate the shunt resistance using Eq. (6.19):  $R_3 = 5.527$  m $\Omega$ .

## 6.6 More than two overdamped junctions

A natural extension of the considerations presented so far in this chapter would be a system of more than two JJs. The equations describing the phase dynamics in a linear array of three and more coupled overdamped weak links can be easily obtained using the same reasoning as the one that led us to Eq. (6.11) and Eq. (6.15). Equations obtained in this way have the same general form as those that we have been analyzing so far, that is the term  $I_i - I_{ci} \sin \phi_i$  multiplied by a coupling constant  $\alpha$  appears in the equation for the time derivative of  $\phi_{i-1}$  and  $\phi_{i+1}$  (assuming nearest-neighbors interaction).

Nerenberg et al. performed simulations of the phase dynamics of a system of three coupled JJs with the equations of motion obtained as described above. They were able to demonstrate chaotic motion in that system [38]. Their work was then extended to the case of linear arrays of more than three junctions, where the existence of both voltage locking [35] and deterministic chaos [39] was demonstrated. It is also known that chaotic phase dynamics can arise in small 2D arrays of overdamped JJs [9].

The system of three overdamped JJs with only a DC bias was especially interesting to us in this work, as it is mathematically minimal with regard to the possibility of exhibiting chaotic phase dynamics (its phase space is three-dimensional). We performed extensive simulations for a system of three identical JJs, but were unable to detect any combinations of the coupling constant  $\alpha$  and the two DC bias currents that would yield negative conductance effects at the remaining junction. The plots of the averaged phase velocity on  $(\alpha, I_i)$  cuts also did not reveal any complex structures, such as those seen in Figure 6.4. A negative result of a numerical scan is never fully conclusive, as it is impossible to scan over possible parameter combinations with infinite accuracy, but our results allow us to pose the conjecture that the system of three overdamped, DC-biased JJs does not exhibit any negative mobility effects. However, our simulations also revealed that this system does exhibit negative mobility when an AC driving is added to at least one of the junctions. On  $(a_1, \omega)$  cuts, the phase dynamics of the driven system was similar to that of two JJs – areas of non-zero mobility of all three particles formed striped structures, and for sufficiently high coupling, islands of negative mobility appeared near the intersections of these strips.

## 7 Summary

In the previous two chapters we demonstrated the existence of different kinds of anomalous transport effects in a single resistively and capacitively shunted Josephson Junction (JJ), as well as in a system of two coupled overdamped JJs. Our findings presented in Chapter 5 fully agree with the results concerning this subject published by other authors [30, 46]. The contents of that chapter can therefore be seen as an independent confirmation of their work. The analysis of negative conductance effects in a system of two externally driven JJs presented in Chapter 6 is to the best of our knowledge novel, and has not been previously published elsewhere.

In both of the analyzed systems we were able to find all of the following anomalous transport effects: Absolute Negative Mobility (ANM), Negative Nonlinear Mobility (NNM), and Negative Differential Mobility (NDM). Depending on the chosen point in the parameter space, the effects were either deterministic in nature, induced by thermal fluctuations, or induced by the coupling between the individual junctions. The second kind is perhaps the most astonishing, as it directly contradicts our intuition about noise always having a destructive influence on any useful effects. We have however found that the noise-induced negative mobility effects could always be explained by referring to the dynamical properties of the noiseless system.

The third result presented in this thesis is a null one – we were unable to detect any negative conductance effects in a system of three identical, overdamped JJs subject only to DC biases. This does not mean that the presence of these effects is completely ruled out though – numerical scans of the parameter space are by its nature done only for a finite range of parameters and have limited precision. In particular, it might be possible to trigger such effects by carefully tailoring the critical currents of the JJs and the coupling between them.

Overall, it seems that negative mobility effects, while quite surprising at first glance, are actually fairly common and robust, given the multiple areas of the parameter spaces where we were able to detect their presence, and given the fact of their survival under moderate thermal fluctuations. When the systems in question are taken to model Brownian particles, the negative mobility effects might find an application in particle sorting, which is an important problem e.g. in microfluidics. For Josephson junctions, the knowledge of detailed I-V characteristics might be useful for the design and operation of some of the many devices built on the basis of the Josephson effect.

Regardless of the practical applications, we also feel that the negative mobility effects

## *7 Summary*

---

are quite interesting in their own right, as they increase our understanding of dynamical systems and challenge commonly held intuitions.

The results presented in this thesis answer some questions and raise a few new ones. Future work on this subject might include a study of the impact of more realistic noise models and different kinds of external driving on the negative mobility effects. Another question is also the presence of these effects in systems of spatially extended arrays of weak links (one-, two-, and three-dimensional). Finally, it would be interesting to try to experimentally confirm the numerical predictions for the system of two coupled JJs presented in Chapter 6.

If the existing results in the field are any indication, we can refer to the following popular principle in physics: „processes that are not forbidden by symmetries and conservation laws have to occur”, and fully expect to find negative mobility effects in more complex systems, where additional adjustable parameters should allow for more fine-grained control. Also, since the anomalous transport effects were found only very recently in a system that has been studied in different contexts for many years, it is very possible that further interesting transport effects remain to be discovered even in simple classical systems – it seems our knowledge is never as complete as we think it to be.

# Appendices

## A The `sdepy` software package

This chapter describes the `sdepy` Python module that was used for all calculations presented in this thesis. The software was developed in parallel with the thesis as an independent open source project, and has been made freely available and published under the LGPL 3.0 license [1].

### A.1 General architecture of `sdepy`

`sdepy` can be seen as an extension of the work presented by Januszewski and Kostur [21] – it is based on the same general ideas of how to use CUDA to numerically solve SDEs (which we already discussed in Chapter 3), but it uses different technologies, which makes it more powerful and flexible. `sdepy` is written using Python and the Mako template language, and makes heavy use of popular Python libraries, such as NumPy, SciPy, SymPy and PyCUDA. The libraries provide access to fast array manipulation routines, basic numerical algorithms, symbolic computation and CUDA devices from within Python scripts.

The primary innovation in `sdepy` is its use of template-based Run-Time Code Generation (RTCG) (similar ideas were recently presented by Klöckner et al. [25]). In `sdepy`, RTCG is used to automatically generate optimized code for a specific system of SDEs. Each problem to be solved using `sdepy` is defined as a Python script. The equations are specified as a block of text, which by itself is a piece of C code. Standardized names are used for dynamical variables: `x0`, ..., `xN` for a system of  $N + 1$  first order SDEs. Every simulation can use an arbitrary number of external parameters, defined as a Python dictionary mapping parameter names to their descriptions. Parameters defined in this way are automatically converted to command line arguments, so that the user can specify their values when starting the simulations. These parameters can also be assigned multiple values, in which case a simulation is run for each of the specified values. Multiple values are specified in the form of ranges `start:stop:steps`, optionally prefixed by the word `log:` if the numbers are to be spaced evenly on the logarithmic scale.

The equations, the external parameters, and a number of other values (such as the number of dynamical variables `num_vars` or the number of Gaussian noises `num_noises`) are used to instantiate an object of the `SDE` class. The `prepare` method of this object is then used to select the algorithm used to solve the equations, set the initial values of all dynamical variables, and optionally specify the system parameter corresponding to

frequency, which is then used to calculate the step size. The step size is never directly specified by the user. Instead, the user provides the `spp` parameter which stands for *steps per period*, and this number together with the value of the frequency variable is used to calculate a suitable step size. This makes it possible to efficiently perform scans over the frequency axis of the parameter space of the system.

Currently, only the stochastic Euler, Milstein and second order Runge-Kutta schemes are supported in `sdepy`. The initial values of the system variables are specified as `numpy` vectors. When the `prepare` method is called, a program in the CUDA C language is automatically generated, compiled, and prepared for execution on the GPU, which entails e.g. copying data from `numpy` arrays on the host to the GPU memory. The CUDA C code is based upon a Mako template file and the options specified by the user when the `SDE` object was created. The code does not contain any superfluous parts – for instance, it only generates the necessary number of normal variates in each iteration.

The actual simulation is started when the `simulate` method of the `SDE` object is called. If multiple values of a system parameter were specified, they are all calculated in parallel on the GPU. If more than one parameter has multiple values, simulations are run for all combinations of the parameter values, and only the parameter with the highest number of values will be scanned over in parallel, while the rest will be serialized on the host. The results of a simulation can be saved to disk as `numpy` arrays or text files, or stored inside a Python object for further processing.

Stochastic simulations typically generate a lot of data, so usually the individual trajectories are not saved. Instead, ensemble averages can be calculated and stored by `sdepy`. Functions for several commonly used values expressible in terms of such averages are provided within the `sde` module (e.g. `avg_moments` to calculate  $\langle x_i \rangle$  and  $\langle x_i^2 \rangle$ , and `diffusion_coefficient` to calculate  $D_{\text{eff}}$ ). `sdepy` supports two output modes selected by the `output_mode` command line parameter: `path` and `summary`. In the first mode, the output data is calculated and saved every `samples` time steps (which is another command line parameter). In the `summary` mode, only the final state of the simulation is used to generate the output data. The latter mode is used e.g. when estimating the average velocity  $\langle v \rangle$ , for which the `drift_velocity` function in the `sde` module can be used. The default output format is a compressed `numpy` array, which is efficient in terms of disk space (the data is saved in binary form), and which can easily be converted into MatLab files. All output files generated by `sdepy` are designed to be self-describing – e.g. they contain the exact command line parameters that were used to generate a particular data set. This is an extremely useful feature in practice, as it makes it easy to identify what a given result file represents and does away with the need of manually describing simulation results in separate text files.

All of the above-mentioned features of `sdepy` are illustrated in Listing 1.

**Listing 1** A sample program using the `sdepy` module. The program numerically solves Eq. (5.4) using the Stochastic Runge-Kutta method of the second order (SRK2).

```

#!/usr/bin/python
import math
import numpy
import sde
import sympy
import sys

def init_vector(sdei, i):
    if i == 0:
        return numpy.random.uniform(0, 2 * math.pi, sdei.num_threads)
    else:
        return numpy.random.uniform(-2, 2, sdei.num_threads)

sim_params = {'force': 'DC bias current',
              'gam': 'damping constant',
              'omega': 'AC drive frequency',
              'd0': 'noise strength',
              'amp': 'AC drive amplitude'}
const_pars = {
    'phi0': lambda sdei: numpy.random.uniform(0, 2 * numpy.pi, sdei.num_threads)}
local_vars = { 'ns': lambda sdei: sympy.sqrt(sdei.S.d0 * sdei.S.dt * 2 * sdei.S.gam) }

code = """
dx0 = x1;
dx1 = -sinf(x0) + amp * cosf(omega * t + phi0) + force - gam * x1;
"""

ns_map = {1: ['ns']}
period_map = {0: sde.PeriodInfo(period=2.0 * math.pi, freq=1)}

sdei = sde.SDE(code, sim_params, num_vars=2, num_noises=1, noise_map=ns_map,
                period_map=period_map, local_vars=local_vars,
                const_pars=const_pars)

output = {'path': {
            'main': [sde.OutputDecl(func=sde.avg_moments, vars=[0])],
            },
            'summary': {
            'main': [sde.OutputDecl(func=sde.drift_velocity, vars=[0])],
            }
            }

sdei.prepare(sde.SRK2, init_vector, freq_var='omega')
sdei.simulate(output)

```

---

## A.2 Optimization techniques

sdepsy uses a number of optimization techniques to ensure that simulations are carried out efficiently. First of all, a large number of independent threads is scheduled for execution on the GPU. The exact number is controlled by the `paths` command line option, which defines the number of independent realizations to be calculated, as well as by the number of system parameter values if a scan over the parameter space of the simulated system is being performed. Such an approach is justified in the CUDA environment, which requires a large number of threads (at least a couple hundred for currently available graphics cards) to fully saturate the hardware resources [40].

The second important optimization strategy is the calculation of multiple iterations of the numerical scheme in a single kernel call. That means that the system advances by several time steps before control is returned to the host, and that some of the results are never seen directly by the user, as they are only stored as intermediate values on the GPU. This is usually acceptable, as the exact dynamics of the system on the scale of individual time steps is seldom important, especially when the asymptotic regime is of primary interest. The number of time steps to be calculated in a single kernel call is specified by the user via the `samples` command line parameter. This optimization technique works in two ways. First, it minimizes the amount of data transferred from the GPU to the host, which is important as the PCI-Express bus over which the data is sent is quite slow in comparison with the internal GPU memory. Second, when multiple iterations are calculated in a single kernel call, system parameters stored in the global memory of the GPU can be cached in local variables, which are much faster, provided there are enough free registers in the multiprocessor [40].

By default, all calculations in sdepsy are performed using single precision floating-point numbers (this can be changed using the `--precision=double` command line option). On currently available GPUs, single precision operations are about an order of magnitude faster than double precision ones. To increase the precision of the calculations without sacrificing performance, sdepsy supports *warping* of dependent and independent variables. Let  $var$  be a variable used in the simulation. If only  $var \bmod p$  is relevant for the system dynamics, sdepsy can be instructed to only pass  $var \bmod p$  to the GPU code, while keeping track of the full value of  $var$  on the host. In the program in Listing 1, this is done for the dynamical variable number 0 (particle position), for which  $p = 2\pi$  as  $x_0$  is only used as an argument of the sine function. Variable warping makes it possible to avoid numerically pathological situations in which a small quantity is added to a much larger one. In single precision, such an operation is problematic if one of the quantities is more than 7 orders of magnitude larger than the other one. An additional advantage of keeping simulation variables small is the increased performance and precision of transcendental functions on the GPU, particularly if the functions are hardware-accelerated by the Special Functions Unit of the SM. We have found that the single precision does

not degrade the results of the calculations if the above precautions are taken [21].

### A.3 Summary and future work

We have found `sdepsy` to be very useful for all calculations presented in this thesis. Thanks to the tremendous computational power of GPUs, we were able to achieve almost a three orders of magnitude speed-up compared to a single modern CPU. `sdepsy`'s integration with popular Python libraries made it easy to postprocess and analyze the data interactively using `numpy` routines, as well as to visualize it with `matplotlib`.

The `sdepsy` Python module has already proven to be quite useful for simple stochastic simulations, but there is still a lot of room for improvement and further development. It would not be difficult to provide an alternative code generator that could use the existing Mako templates to generate OpenCL code instead of CUDA C. This would make it possible to run `sdepsy` on a wider range of hardware, as OpenCL is supported on many devices, while CUDA is limited to NVIDIA GPUs. In practice, CUDA is currently usually a few times faster, but this is likely to improve as different OpenCL implementations mature.

Furthermore, it might be worthwhile to make more extensive use of the `sympy` module for code generation purposes. Currently, `sympy` is only used to define additional local variables. These variables are then either evaluated completely on the host, if they only depend on constant quantities, or calculated in each thread otherwise. If the equations to be solved would themselves be `sympy` expressions, it should be possible to automatically generate optimized code for their numerical solutions using more accurate stochastic integration schemes than the ones already implemented. These schemes have better convergence properties, but they also use lengthy formulas, which can sometimes be simplified in special cases (e.g. if all the noises are additive) [26]. `sympy` could make it possible to automatically adjust the numerical schemes to the specific problems that the user wants to solve, without requiring any manual calculations which are always prone to errors.

## Bibliography

- [1] The sdepsy project repository. <http://gitorious.org/sdepsy/>.
- [2] A. Barone and G. Paternò. *Physics and Applications of the Josephson Effect*. John Wiley & Sons, New York, 1982.
- [3] F. Beichelt and P. Fatti. *Stochastic Processes And Their Applications*. CRC Press, October 2001. ISBN 0415272327.
- [4] Wu Binruo, Yang Zhou-jing, J. A. Blackburn, S. Vik, H. J. T. Smith, and M. A. H. Nerenberg. Analog simulation of coupled superconducting weak links: Locking and chaos. *Phys. Rev. B*, 37(7):3349–3358, Mar 1988. doi: 10.1103/PhysRevB.37.3349.
- [5] A. C. Brańka and D. M. Heyes. Algorithms for Brownian dynamics simulation. *Phys. Rev. E*, 58(2):2611–2615, Aug 1998. doi: 10.1103/PhysRevE.58.2611.
- [6] A. C. Brańka and D. M. Heyes. Algorithms for Brownian dynamics computer simulations: Multivariable case. *Phys. Rev. E*, 60(2):2381–2387, Aug 1999. doi: 10.1103/PhysRevE.60.2381.
- [7] K. Burrage, P. Burrage, D. J. Higham, P. E. Kloeden, and E. Platen. Comment on “numerical methods for stochastic differential equations”. *Phys. Rev. E*, 74(6):068701, Dec 2006. doi: 10.1103/PhysRevE.74.068701.
- [8] C. C. Chi and C. Vanneste. Onset of chaos and dc current-voltage characteristics of rf-driven Josephson junctions in the low-frequency regime. *Phys. Rev. B*, 42(16):9875–9895, Dec 1990. doi: 10.1103/PhysRevB.42.9875.
- [9] J. S. Chung, K. H. Lee, and D. Stroud. Dynamical properties of superconducting arrays. *Phys. Rev. B*, 40(10):6570–6580, Oct 1989. doi: 10.1103/PhysRevB.40.6570.
- [10] P. Crotty, D. Schult, and K. Segall. Josephson junction simulation of neurons. *ArXiv e-prints*, February 2010.
- [11] A. S. Deakin and M. A. H. Nerenberg. Uniform expansions for nearly locked coupled Josephson weak links. *Phys. Rev. B*, 25(3):1559–1564, Feb 1982. doi: 10.1103/PhysRevB.25.1559.

## Bibliography

---

- [12] R. Eichhorn, P. Reimann, and P. Hänggi. Absolute negative mobility and current reversals of a meandering Brownian particle. *Physica A: Statistical Mechanics and its Applications*, 325(1-2):101 – 109, 2003. ISSN 0378-4371. doi: DOI:10.1016/S0378-4371(03)00188-2. Stochastic Systems: From Randomness to Complexity.
- [13] R. Feynman. *The Feynman Lectures on Physics: Volume 3*. Addison-Wesley, Boston, 1963.
- [14] C. W. Gardiner. *Handbook of Stochastic Methods: For Physics, Chemistry and the Natural Sciences (Springer Series in Synergetics)*. Springer, November 1996. ISBN 3540616349.
- [15] A. A. Golubov, M. Yu. Kupriyanov, and E. Il'ichev. The current-phase relation in Josephson junctions. *Rev. Mod. Phys.*, 76(2):411–469, Apr 2004. doi: 10.1103/RevModPhys.76.411.
- [16] A. Haljas, R. Mankin, A. Sauga, and E. Reiter. Anomalous mobility of Brownian particles in a tilted symmetric sawtooth potential. *Phys. Rev. E*, 70(4):041107, Oct 2004. doi: 10.1103/PhysRevE.70.041107.
- [17] J. Bindslev Hansen and P. E. Lindelof. Static and dynamic interactions between Josephson junctions. *Rev. Mod. Phys.*, 56(3):431–459, Jul 1984. doi: 10.1103/RevModPhys.56.431.
- [18] R. L. Honeycutt. Stochastic Runge-Kutta algorithms. I. White noise. *Phys. Rev. A*, 45(2):600–603, Jan 1992. doi: 10.1103/PhysRevA.45.600.
- [19] R. A. Hopfel, J. Shah, P. A. Wolff, and A. C. Gossard. Negative absolute mobility of holes in n-doped GaAs quantum wells. *Applied Physics Letters*, 49(10):572–574, 1986. doi: 10.1063/1.97044.
- [20] M. Iansiti, Qing Hu, R. M. Westervelt, and M. Tinkham. Noise and Chaos in a Fractal Basin Boundary Regime of a Josephson Junction. *Phys. Rev. Lett.*, 55(7):746–749, Aug 1985. doi: 10.1103/PhysRevLett.55.746.
- [21] M. Januszewski and M. Kostur. Accelerating numerical solution of stochastic differential equations with CUDA. *Computer Physics Communications*, 181(1):183 – 188, 2010. ISSN 0010-4655. doi: DOI:10.1016/j.cpc.2009.09.009.
- [22] D. W. Jillie, M. A. H. Nerenberg, and J. A. Blackburn. Voltage locking and other interactions in coupled superconducting weak links. II. Experiment. *Phys. Rev. B*, 21(1):125–131, Jan 1980. doi: 10.1103/PhysRevB.21.125.
- [23] R. L. Kautz. Noise, chaos, and the Josephson voltage standard. *Reports on Progress in Physics*, 59(8):935, 1996.

## Bibliography

---

- [24] A. J. Kerman. Metastable Superconducting Qubit. *Phys. Rev. Lett.*, 104(2):027002, Jan 2010. doi: 10.1103/PhysRevLett.104.027002.
- [25] A. Klöckner, N. Pinto, Y. Lee, B. C. Catanzaro, P. Ivanov, and A. Fasih. Py-CUDA: GPU Run-Time Code Generation for High-Performance Computing. *CoRR*, abs/0911.3456, 2009.
- [26] P. E. Kloeden and E. Platen. *Numerical solution of stochastic differential equations*. Springer-Verlag, Berlin ; New York :, 1992. ISBN 3540540628 0387540628.
- [27] M. Kostur, L. Machura, P. Talkner, P. Hänggi, and J. Łuczka. Anomalous transport in biased ac-driven Josephson junctions: Negative conductances. *Phys. Rev. B*, 77(10):104509, Mar 2008. doi: 10.1103/PhysRevB.77.104509.
- [28] M. Kostur, J. Łuczka, and P. Hänggi. Negative mobility induced by colored thermal fluctuations. *Phys. Rev. E*, 80(5):051121, Nov 2009. doi: 10.1103/PhysRevE.80.051121.
- [29] K. K. Likharev. *Dynamics of Josephson Junctions and Circuits*. Gordon and Breach, New York, 1986.
- [30] L. Machura, M. Kostur, P. Talkner, J. Łuczka, and P. Hänggi. Absolute Negative Mobility Induced by Thermal Equilibrium Fluctuations. *Phys. Rev. Lett.*, 98(4):040601, Jan 2007. doi: 10.1103/PhysRevLett.98.040601.
- [31] Y. Makhlin, G. Schön, and A. Shnirman. Quantum-state engineering with Josephson-junction devices. *Rev. Mod. Phys.*, 73(2):357–400, May 2001. doi: 10.1103/RevModPhys.73.357.
- [32] G. E. Moore. Cramming more components onto integrated circuits. *Electronics*, 38(8):4–8, Apr 1965.
- [33] A. Naess and V. Moe. Efficient path integration methods for nonlinear dynamic systems. *Probabilistic Engineering Mechanics*, 15(2):221 – 231, 2000. ISSN 0266-8920. doi: DOI:10.1016/S0266-8920(99)00031-4.
- [34] J. Nagel, D. Speer, T. Gaber, A. Sterck, R. Eichhorn, P. Reimann, K. Ilin, M. Siegel, D. Koelle, and R. Kleiner. Observation of Negative Absolute Resistance in a Josephson Junction. *Phys. Rev. Lett.*, 100(21):217001, May 2008. doi: 10.1103/PhysRevLett.100.217001.
- [35] M. A. H. Nerenberg and J. A. Blackburn. Mutual voltage locking in linear arrays of Josephson weak links. *Phys. Rev. B*, 23(3):1149–1155, Feb 1981. doi: 10.1103/PhysRevB.23.1149.

## Bibliography

---

- [36] M. A. H. Nerenberg, J. A. Blackburn, and D. W. Jillie. Voltage locking and other interactions in coupled superconducting weak links. I. Theory. *Phys. Rev. B*, 21(1): 118–124, Jan 1980. doi: 10.1103/PhysRevB.21.118.
- [37] M. A. H. Nerenberg, J. A. Blackburn, and S. Vik. Chaotic behavior in coupled superconducting weak links. *Phys. Rev. B*, 30(9):5084–5088, Nov 1984. doi: 10.1103/PhysRevB.30.5084.
- [38] M. A. H. Nerenberg, J. H. Baskey, and J. A. Blackburn. Chaotic behavior in an array of coupled Josephson weak links. *Phys. Rev. B*, 36(16):8333–8337, Dec 1987. doi: 10.1103/PhysRevB.36.8333.
- [39] M. A. H. Nerenberg, R. J. Spiteri, and J. A. Blackburn. Chaos in extended linear arrays of Josephson weak links. *Phys. Rev. B*, 40(16):11294–11296, Dec 1989. doi: 10.1103/PhysRevB.40.11294.
- [40] NVIDIA Corporation. NVIDIA CUDA Programming Guide, version 3.0, 2010. URL [http://developer.download.nvidia.com/compute/cuda/3\\_0/toolkit/docs/NVIDIA\\_CUDA\\_ProgrammingGuide.pdf](http://developer.download.nvidia.com/compute/cuda/3_0/toolkit/docs/NVIDIA_CUDA_ProgrammingGuide.pdf).
- [41] H. Nyquist. Thermal Agitation of Electric Charge in Conductors. *Phys. Rev.*, 32(1):110–113, Jul 1928. doi: 10.1103/PhysRev.32.110.
- [42] E. Ott. *Chaos in Dynamical Systems*. Cambridge University Press, 2nd edition, September 2002. ISBN 0521010845.
- [43] T. Pang. *An Introduction to Computational Physics*. Cambridge University Press, 2nd edition, February 2006. ISBN 0521825695.
- [44] M. Pharr and R. Fernando. *GPU Gems 2: Programming Techniques for High-Performance Graphics and General-Purpose Computation (Gpu Gems)*. Addison-Wesley Professional, 2005. ISBN 0321335597.
- [45] H. Risken. *The Fokker-Planck Equation: Methods of Solutions and Applications*. Springer Series in Synergetics. Springer, 2nd ed. 1989. 3rd printing edition, September 1996. ISBN 354061530X.
- [46] D. Speer, R. Eichhorn, and P. Reimann. Transient chaos induces anomalous transport properties of an underdamped Brownian particle. *Phys. Rev. E*, 76(5):051110, Nov 2007. doi: 10.1103/PhysRevE.76.051110.
- [47] B. N. Taylor, W. H. Parker, and D. N. Langenberg. Determination of  $\frac{e}{h}$ , Using Macroscopic Quantum Phase Coherence in Superconductors: Implications for Quantum Electrodynamics and the Fundamental Physical Constants. *Rev. Mod. Phys.*, 41(3):375–496, Jul 1969. doi: 10.1103/RevModPhys.41.375.